Republic of Iraq
Ministry of Higher Education & Scientific Research
University of Babylon
College of Education for Pure Sciences
Department of Physics

Effect of Strain on the Electronic and Optical properties of AlBrX (X=S, Se) Monolayers .

A Thesis

Submitted to the Council of the College of Education for Pure Sciences at University of Babylon in Partial Fulfillment of the Requirements for the Degree of Master in Education / Physics

by

Suhad Tareq Yousif Dahash

B.Sc. in physics

(University of Baghdad, 2005)

Supervised by

Prof. Hamad R. Jappor (Ph.D) **Assist Prof. Ali O. Muhsen (Ph.D)**

2022 A.D. **1443A.H.**

بسم الله الرحمن الرحيم

﴿وَلِيَعْلَمَ الَّذِينَ أُوتُوا الْعِلْمَ أَنَّهُ الْحَقُّ مِن رَّبِّكَ

فَيُؤْمِنُوا بِهِ فَتُخْبِتَ لَهُ قُلُوبُهُمْ

وَإِنَّ اللَّهَ لَهَادِ الَّذِينَ آمَنُوا إِلَى صِرَاطٍ مُّسْتَقِيمٍ﴾

صدق الله العلي العظيم

سورة الحج ، ايه (54)

Dedications

To the glad tidings the warner and the luminous lamp, who with his guidance illuminated the darkness of ignorance, corruption, injustice and tyranny, so his Lord swore by his right and said, addressing: (لَعَمْرُكَ إِنَّهُمْ لَفِي سَكْرَتِهِمْ يَعْمَهُونَ)

To the Noble Prophet Muhammad and his good and pure family...

And to those who followed his path and believed what God had covenanted with him.

The martyrs of Iraq and the Popular Mobilization Forces (PMF), without whom we would not have enjoyed the blessing of security and safety.

And to those who were the reason for my existence in this life and those who taught me the love of his Prophet and his family (may God's prayers and peace be upon them all) and the love of those who love them, to you, my mother and father, I dedicate the fruit of my humble efforts.

Acknowledgments

Praise be to *Allah*, the Most High, a great, good, and blessed thank you, full of the heavens and the earth, for what He has honored me with in completing this study, which I hope you will be pleased with.

I am pleased to express my gratitude to my Supervisors (*Prof. Dr. Hamad R. Jappor*) and (*Assist Prof. Dr. Ali O. Muhsen*) for their competent guidance, and valuable suggestions.They also helped by sending references and resources required at every stage. I am sure that this work would have never become truth, without their guidance.

Special thanks to the Dean of College of Education for Pure Sciences/university of Babylon and the Department of Physics for their kind help to complete my research.

I would also like to thank all my friends, who have been supportive throughout the preparation of my thesis, and I would like to express my sincere thanks to my family, my brothers (Ahmed, Ali) and especially the younger of them Baqer and my sisters (Rehab, Thekraiat, Ghufran, Samah and Huda) for their generous support that they have given me throughout My life, because of their unconditional love and prayers, I have the opportunity to complete this thesis.

Suhad

Abstract

In the present study,The effect of biaxial strains on the structural, optoelectronic, and photocatalysis properties of AlBrSe and AlBrSe monolayers was investigated by density functional theory (DFT) employing general gradient approximation (GGA) with hybrid functional the materials studio program has been used to design two-dimensional (2D) monolayer materials AlBrSe and AlBrS for the first time with orthorhombic lattices.Perdew–Burke-Ernzerhof (PBE) and Heyd–Scuseria–Ernzerhof (HSE) functionals. The phonon dispersion curve and molecular dynamics simulation indicated that the AlBrSe and AlBrS monolayers are mechanically and thermodynamically stable with the absence of negative values in frequencies. It is found that the AlBrSe monolayer is an indirect semiconductor with bandgaps of 1.654 eV/2.231 eV, whereas the AlBrS monolayer possesses direct bandgaps of 2.221 eV/3.039 eV using PBE and HSE06 methods, respectively. Under the effect of strain, the band gaps range from 1.837 eV to 2.353 eV of AlBrSe, while the band gaps of AlBrS range from 2.933 eV to 3.034 eV. Also, the modified under strain engineering, and a dramatic transformation from indirect to direct bandgap is predicted at tensile strains (4% and 6%). On the other hand, the direct band gaps of the AlBrS monolayer maintain their position at the Γ point during the applied strain. The maximum value of the absorption coefficient located in the ultraviolet region for the two monolayers, while the absorption coefficient in the visible region of AlBrSe is equal to 6.13×10^{3} cm^{-1} at an energy of 3.13 eV and for AlBrS is equal to $1.6\times10^{3}cm^{-1}$ at 3.15 eV. The optical conductivity peak at the pristine state of AlBrSe is about $2.41\times10^{15}\ s^{-1}$ at an energy of 7.53 eV, while it equals $3.65\times10^{-15}\ s^{-1}$ at an energy of 7.83 eV for AlBrS monolayers.

Under the impact of strain, the absorption coefficient and optical conductivity of the two monolayers behave similarly: they grow when compressed and reach their highest values at -6 %, and they drop when tensile and reach their lowest values at 6 %. Moreover, the use of AlBrSe and AlBrS monolayers in innovative energy systems has a bright future as a promising candidate for photocatalytic water-splitting.

List of Contents

List of Figures

List of Abbreviations

Abbreviations	Description
0D	Zero-Dimensional
1D	One-Dimensional
2D	Two-Dimensional
3D	Three-Dimensional
TMDs	transition metals dichalcogenides
IIIA	The thirteen group in the periodic table
VIA	The sixth group in the periodic table
VIIA	The seventh group in the periodic table
(2-DTMDCH)	Two-Dimensional Transition Metal Dichalcogenides Dihalogens
AIMD	Ab Initio Molecular Dynamic
Al	Aluminum
Br	Bromide
S	Sulfur
Se	Selenium
CASTEP	Cambridge Sequential Total Energy Package
CBM	Conduction Band Minimum
DFT	Density Functional Theory
DOS	Density of States
E_F	The Fermi Level
E_{vac}	The Vacuum Level
FP-APW+lo	The Full Potential Augmented Plane Waves Plus level orbitals
GGA	Generalized Gradient Approximation

H	Hydrogen
HF	Hartree-Fock
HK	Hohenberg–Kohn
HSE 06	Heyd-Scuseria-Ernzerhof 2006
IR	Infrared
LCAO	Linear Combination Atomic Orbital
LDA	Local Density Approximation
LSDA	Local Spin Density Approximation
MO	Molecular Orbital
PBE	Perdew, Burke and Ernzerhof
PBESOL	Perdew-Burke-Ernzerhof Revised for Solids
PDOS	Partial Density of States
PW-PP	Plane-Wave Pseudo-Potential Method
SCF	Self-Consistent Field
TDOS	Total Density of States
TMDs	Transition Metals Dichalcogenides
UV	Ultraviolet
VIS	Visible Light
VBM	Valence Band Maximum
VdW	van der Waals
W	Work Function

List of Symbols

Symbols	Definition
Ψ	Wave Function
$\hat{H}$	Hamiltonian operator
$\hat{E}$	Total Energy
$\hat{T}$	Kinetic energy operator
$\hat{T}_e$	Kinetic energy operator for the electrons
$\hat{T}_n$	Kinetic energy operator for the nuclei
$\hat{V}_{ne}$	Potential energy between electron-nucleus
$\hat{V}_{ee}$	Potential energy between electron-electron
$\hat{V}_{nn}$	Potential energy between nucleus-nucleus
$\hbar$	Planck's constant /2π
∇^2	Laplacian operator
m_i	Mass of electron
M_A	Mass of nucleus
E	Electron charge
ε_o	Vacuum permittivity
Z_{AB}	Charge of nuclei A and B
r_{Ia}	Distance between electron I and nucleus a
r_{IJ}	Distance between electron I and electron J
R_{AB}	Distance between A nucleus and B nucleus
$V(r, R)$	The potential energy of all electrons and nuclei
a_o	Bohr radius
$\hat{H}_{tot}$	Total Hamiltonian operator
Ψ_{tot}	Total wave function
Φ	Trial wave function

E_o	Ground-state energy
α	Spin up wave function
β	Spin down wave function
N	Normalization factor
Ψ_i	Molecular orbitals
$\hat{F}$	Fock operator
ε_i	The electronic energy
H	Planck's constant
$\hat{J}_l$	Coulomb operator
$\hat{K}_l$	Exchange operator
Φ_μ	Basis functions
$C_{\mu i}$	The expansion coefficients
M	Number of the basic functions
$\rho(\vec{r})$	Electron density
$V_{ext}(r)$	External potential
$E_{NC}[\rho]$	Non-Classical Energy
$J[\rho_0]$	Classical Coulomb energy
$F_{HK}[\rho]$	Hohenberg-Kohn operator
$T_S[\rho]$	The kinetic energy of no interacting electron system
$E_{xc}[\rho]$	Exchange-correlation energy
δE	The variation of E
$\phi_i(r)$	Kohn–Sham orbital's
$V_{xc}[r]$	Exchange-correlation potential
φ^λ	Wave function to the Hamilton operator
$\bar{\rho}_{xc}$	The averaged exchange-correlation density
$\bar{h}(r_1, r_2)$	The averaged pair correlation function
$\rho\,^{\lambda}_{2}(r_1, r_2)$	The diagonal part of the two-particle density matrix

E_c^{ks}	The Hartree–Fock exchange energy
Ψ_ρ	The exact interacting wave function
ε_{xc}	The exchange-correlation energy
ρ_α	The density of spin-up
ρ_β	The density of spin-down
r_s	The local value of the density parameter
$(n^{\downarrow} - n^{\uparrow})\ /n$	The spin polarization
T	dimensionless gradient
ξ, ζ	Orbital exponent
N	Principal quantum number
l	Orbital quantum number
M	Magnetic quantum number
θ, φ	Polar angles
L	Length of the 1D system
Δn	The difference in the refractive index values
E_b	Binding energies
$\varepsilon\ (\omega)$	Dielectric function
χ	The electronegativity
(a, b, and c)	The number of atoms of an element in the monolayer
E_{CB}	The conduction band
E_{VB}	The valence bands
E_g	Indirect bandgap
E_e	Absolute vacuum scale for normal hydrogen electrode
ε_1	The real component of the dielectric function
ε_2	The imaginary component of the dielectric function

Chapter One

Introduction and Literature Review

1.1 General Introduction

Nanoscience is primarily concerned with the synthesis, characterization investigation, and exploitation of nanostructured materials, as well as their applications. These materials have at least one dimension in the nanoscale range that distinguishes them from one another. A nanometer (nm) is a billionth of a meter, or 10^{-9} meters, in length and width [1]. The nanotechnology term derives from two words combined: the Greek Nanos which means dwarf or Greek numerical initiator nano that points out to a billionth [2]. Due to the developed new techniques, it has become possible to make materials with a dimensional control close to interatomic spacing**.** The obtained new materials, called nanostructured materials, have small dimensions and remarkable physical properties. Nanostructure science and technology is a large and interdisciplinary area of research that has grown explosively in recent years all over the world due to the rapid advancement of nanotechnology which will assuredly increase in the future [3]. It is a proven fact that each class of nanomaterials possesses previously unheard-of characteristics that arise from their size. If one dimension is restricted, a layered shape or two-dimension(2D) material can be made, if two dimensions are constrained can be found of one dimension material (1D), if all dimensions are constrained, it is called zero-dimension material (0D), Preeminent was graphite(3D), Fullerenes (0D), followed by nanotubes (1D), and graphene (2D) [4,5]. These materials cover various types of nanostructures, which includes metallic, semiconducting, ceramic, etc, which have the structural features between those of atoms and the bulk materials. This field is an excellent example of how pure science and technology interact and influence one another [6]. Modelling and simulations are some of the important basics of computational nanotechnology. Because of the cost of research laboratories and the

sluggishness of the experimentation practicability, it may not be safe to depend on experimental nanotechnology only. Some considered that simulations and modelling is a computational experiment.The computational interrogator has control over all the forces that could impact the properties, structure, and dynamics of nanomaterials and the mastery to implement a systematic study of the actions and reactions of all forces [7]. That is, a theoretical sample is designed completely similar to the original sample, and then the engineering improvement is carried out to simulate the properties of the designed sample according to theoretical programs and functions through which we can predict the nature of materials and their applications, that may be difficult to design or create at present due to the absence of practical equipment or high cost [8].

1.2 Two-Dimensional Monolayer Materials

To define“ultrathin two-dimensional (2D)" its lateral size is more than 100 nm and its thickness typically is less than 5 nm [9] in addition to vertical weak van der Waals (vdW) interactions sandwiched among the neighboring sheets [10]. In 2004, Novoselov and his associates successfully exfoliated ultrathin nanomaterial (graphene) from graphite using scotch tape now defined as micromechanical cleavage considered tremendous equipment, and a great scientific solution in the manufacture of 2D-nanomaterials [11]. now defined it as micromechanical cleavage. Two-dimensional features provide a broad range of physical, electronic, and chemical properties that are superior to those of conventional materials. As a result, there has recently been considerable interest in discussing the unique properties of ultrathin 2D nanomaterials from a variety of perspectives. One advantage of ultrathin 2D nanomaterials without interlayer interactions is that they exhibit significantly superior electronic

properties when compared to other types of nanomaterials. This makes them attractive candidates for fundamental condensed matter research as well as electronic applications in the first instance [10]. Second, because of their atomic thickness, they have the greatest mechanical flexibility and optical transparency of any material, making them particularly promising for the creation of very flexible and transparent electrical and optoelectronic applications. Finally, because of their huge lateral size and ultrathin thickness, they have an extremely high specific surface area, making them particularly well suited for surface-active applications [12]. 2D nanostructures are foreseen to have a significant impact on a tremendous assorted variety of utilizations, stretching from electronics, and high execution sensors to gas storage or separation, support membranes and catalysis, inert coatings, and so on. At the moment, not just the carbon materials from the 2D materials family but likewise transition metals dichalcogenides (TMDs) and layered metal oxides are all 2D layered [13,14].

At long last, materials with a hexagonal structure, such as Graphene, have the potential to be used in a wide range of applications, such as skimming spectroscopy probes, electronic sensing and attractive plans, and solar technology. These accompanying nanofilms, which tin can disclose confrontation, efficiency, with self-inductance fast, have the potential to be used in nonlinear optics, solar technology, and nonlinear optics, among others. After a slew of beautiful features was discovered in these materials, they became the primary source of inspiration for further scientific investigation as well as a potential material for use in contemporary practical applications [15].

1-3 Effects of Strain

The stress impact on transport in semiconductors has been a study topic for more than a half-century. To elucidate the phenomenon, Bardeen and Shockley proposed the deformation potential hypothesis in the early 1950s [16]. Herring and Vogt were extended to represent the interaction of electrons and acoustic waves in materials and to express relaxation durations through the potential of active mass and deformation [17].

Strain directly affects the total energy of the compound to be measured, and this, in turn, generates a significant change in the optical properties based on changes in the electronic structure, thus opening up broad horizons of potential applications in the field of optoelectronics [18]. It is also used to explain the mobility improvement caused by uniaxial stress, it is only true for uniaxial stress in the direction of [001] or equivalently, for a model that is strained biaxially or in-plane [19]. 2D nanomaterials are especially useful for strain-designed structures because they can withstand more strain and may thus be modified by altering bond lengths, angles, and relative atomic configurations e.g molecules and atoms [20]

1.4 Photocatalysis

One of the most promising ways to generate clean or environmentally friendly energy is through the use of photocatalysts. The photocatalysts may be used not only for generating energy but also for water sterilization and air purification, etc. [21,22]. The increasing demand for energy production due to the increase in population growth and the widespread electronics in all life facilities stimulated researchers to search or investigate new sources to support the existing energy represented by fossil fuels and natural gas [23,24]. Hydrogen is considered one of the most important and domestic replacements for fossil oils because it does not

create greenhouse gases such as CO_2 but because it is a sustainable form of energy. Hydrogen fuel can be obtained from water splitting by photocatalysis. Harness semiconductor materials for this purpose [25]. Throughout the process of absorbing the photon energy larger than or equal to the energy gap, this energy is absorbed by the electrons, who then migrate from the valence band to the conduction band, leaving a gap, and therefore during this process, large numbers of excitons will be created. After the generation of excitons, the semiconductor becomes effective for the water-splitting process, and the formation of gaseous oxygen (equation 1.1) and hydrogen (equivalence 2) results from the oxidation of adsorbed water molecules and the reduction of protons [26].

Oxidation: $H_2O + 2h^+ \rightarrow 2H^+ + \frac{1}{2}O_2$ (1.1)

Reduction: $2H^+ + 2e^-$ (1.2)

The most important necessary conditions that must be met in a semiconductor for it to be adopted as a photocatalyst for hydrogen production are as follows [27–29]:

1. The energy arrays from 1.230 eV to 3.30 eV.

2. The conduction band edge should have a greater potential; greater than the reduction band's leading edge at H^{++} // H_2 (-4.441 eV).

3. The valence band edge would stand lesser than the oxidation potential at O_2 / H_2O (-5..670 eV).

1.5 $Al_2Br_2Se_2$ and $Al_2Br_2S_2$ Monolayer Materials

Very recently, aluminum-based 2D materials have emerged as attractive materials for various applications due to their high dynamic and mechanical stability, wide absorption range, excellent thermoelectric performance, high carrier mobility, appropriate band alignment, low Gibbs free energy, and suitable bandgap [30–33]. This makes aluminum-based 2D materials an extraordinary candidate in a large number of applications, including optoelectronic [34], construction of thermoelectric devices [35,36], microelectronics, water splitting, and nanoscale electromechanical [37,38]. For example, it was found that 2D layered AlX (X = S, Se, Te) materials can be used as promising for high-performance thermoelectric materials with an optimized figure of merit parameter of AlTe, AlSe, and AlS monolayers as 0.26, 0.59, and 0.52 respectively [39]. Furthermore, aluminum oxide nanosheets are shown to be dynamically stable and have large band gaps which makes them suitable for photodetectors and light-emitting diodes [40,41]. In the present work, two layers have been designed that include the transitional metals represented by aluminum (Al), the chalcogen represented by sulfur (S) and selenium (Se), and the halogens represented by bromine (Br). The atomic number of Al is 13, and it is located within the thirteenth group (IIIA) and has widespread in the earth's crust, meaning it comes after the element iron in terms of abundance in nature. While S and Se have atomic numbers of 16 and 34 respectively, they are located within the sixteenth group (VIA) in the periodic table of the elements and are highly abundant in nature, and are cheap. Whereas, Br is in group seventh (VIIA), with an atomic number of 35. With this wonderful combination of elements, new properties can be obtained that enable these layers to play an ideal role in various applied fields. A primitive cell contains two atoms for each element as shown in Fig (1.1), so

the chemical formula for these layers will be in the following order $Al_2Br_2S_2$ and $Al_2Br_2Se_2$. This work studied Two-Dimensional Transition Metal Dichalcogenides Dihalogens (2-DTMDCH) with an orthorhombic lattice as a new family of 2D materials. The lattice parameters of $Al_2Br_2S_2$ are a=3.509Å, and b= 4.824 Å while for $Al_2Br_2Se_2$ are a=3.585 Å, b=5.134 Å, and c=27 Å for each monolayer to prohibit interaction between adjacent layers. Atoms in a monolayer are linked by strong covalent bonds, while the bonding forces between adjacent layers are weak Vander Waals forces. Br atoms are distributed on both sides of the monolayer from the top and bottom, and this is clearly shown in Fig. (1.1 b,d) of the layers. The atoms of Al, S, and Se are located in the middle of the layer and are distributed successively. In general, the properties of two-dimensional materials can be modified or controlled by replacing atoms, exposing them to strain, electric field, doping, or through defects within the layer to obtain new properties that differ from those in the usual case and to cover a wider range of applications required in the fields of science different.

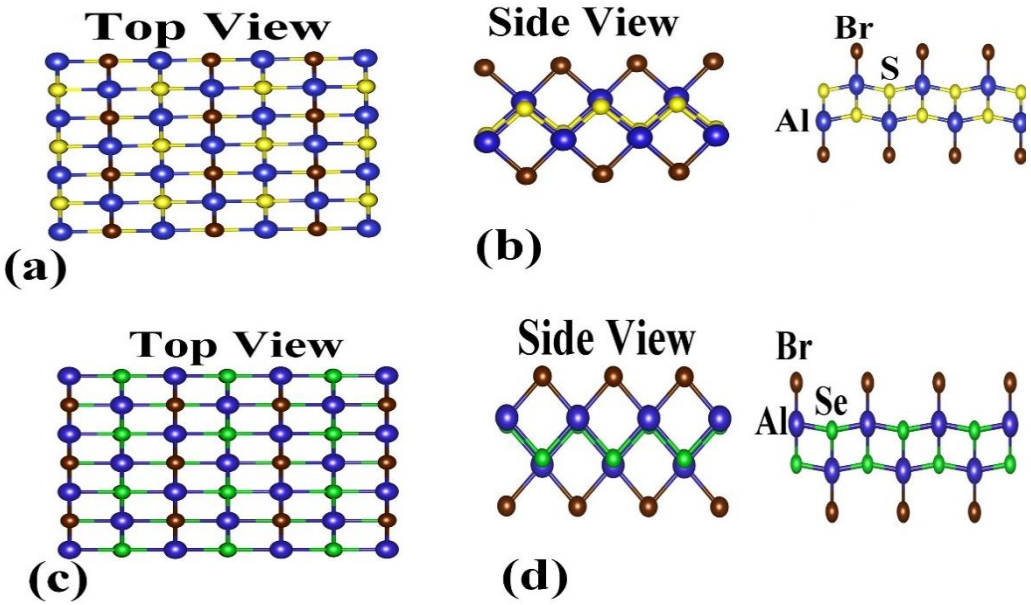

Fig. (1.1) The optimized structure of the highest with sideways opinions of (a), and (b) $Al_2Br_2S_2$, (c) and (d) $Al_2Br_2Se_2$ monolayer.

1.6 Previous Studies

Y. Ma *et al*. in 2014 [42] focused on the monolayer possessing enormous Rashba spin splitting and the appearance of the electrical polarity of BiTeX(X=Br with I) monolayers, where they used first-principles calculations. They predicted the steady Bi-Te-X (X = Br with I) sheets have a significant polar electric playing field in the plane's usual route, creating two-dimensional polar systems. Furthermore, they discover that these new monolayers with thicknesses as little as 3.80 may generate a massive Rashba spin splitting due to their unusually polar atomic arrangements. Furthermore, they indicate that strain can efficiently control the Rashba characteristics of BiTeX monolayers.

S. Wen *et al*. in 2015 [43] studied the effects of hydrogenation, tension, and electronic properties of single layers of tin (SnX_2, X= S, Se, Te) through preliminary calculations based on the (DFT) theory. They found that the single-layer SnX_2 depending on the state of the Sn-X bond could be either a semi-conductor or an intrinsic metal. They also showed that by applying tension, a single layer with adjustable bandgap and electronvolt en metallic properties could be achieved. They predicted that these tin-based di-chalcogenide monolayers with multiple controllable functions could be used in nanoscale devices and sensors.

M. Gonzalez and I. Oleynik in 2016 [44] used the DFT system to calculate the electronic, vibration, and structural characteristics of SnS_2 and $SnSe_2$. They clarified that the structural characteristics of both SnS2 and SnSe2, including lattice parameters in the plane, interstitial spaces, and bound energies significantly affect optoelectronic properties. They revealed the monolayers of SnS_2 and $SnSe_2$ have An indirect bandgap which equals 2.41 and 1.69 eV respectively. Also, proved that it can be used Raman spectra exhibit a substantial reduction in Raman intensity when reducing

the number of layers to a monolayer to determine the number of layers in a 2D sample.

M. Safari *et al*. in 2017 [45] used the full potential augmented plane waves plus local orbitals (FP-APW+lo) approach to investigate the structural, electrical, and optical features of ZnX and CdX (X=S, Se, with Te) mixes in a 2D graphene-like construction. These two compounds retain the essence of their direct bandgap and are thus optically active. For these monolayers, the static dielectric constants reflect a growing trend with a decrease in bandgap values. The findings given in their research demonstrated that ZnS and CdS may be employed effectively in optoelectronic strategies.

X. Lv. X *et al*. in 2017 [27] proposed the usage of 2D germanium monochalcogenides with great carrier mobility during water splitting photocatalytic, after validating the durability of phosphorene like germanium monochalcogenides monolayers (GeS with GeSe), Heyd–Scuseria–Ernzerhof (HSE) hybrid functional revealed that GeS has an indirect bandgap of 2.290 e V and GeSe has direct band-gap at 1.590 eV. Using deformation potential theory, large and directionally anisotropic carrier mobilities (2430.500 $cm^2V^{-1}s^{-1}$ for GeS and 4032.640 $cm^2\ V^{-1}\ s^{-1}$ for GeSe) are quantitatively studied. Furthermore, the holes and electrons in GeS and GeSe monolayers were well separated, thus reducing photocatalytic action with great efficiency. The group structure could be changed from semiconductor to metal using strain, and a direct-indirect bandgap transition could be detected. They can be effectively tailored to meet the reduction and oxidation-reduction potential requirement in water splitting by band gaps and band edge alignment at a specific pH rate. Effectively tuned to meet the requirement at the Oxidation and reduction potential in water splitting.

B. Wang *et al*. in 2018 [46] used the first-principles computations were used to investigate the electrical and optical characteristics of ultrathin Bi_2Te_2S and Bi_2Te_2Se and good electronic mobilities. These monolayers have reasonable band gaps (0.70 electronVolt) within height electron mobilities, which suggests that they can be easily exfoliated from bulk structures. Furthermore, the Bi_2-Te_2-S and Bi_2-Te_2-Se sheets have moderate band gaps (0.7 eV) within height electron mobilities (20,000 $cm^2V^{-1}s^{-1}$, respectively), and they can absorb sunlight efficiently through the whole incident solar spectrum.

X. Chen *et al*. in 2019 [39] used the (DFT) in conjunction with Boltzmann transport theory was used to study the electronic properties of AlX (X = S, Se, Te). In the presence of a dielectric, they exhibited the electronic and phonon of AlX (X = S, Se, Te) sheets. There is a shrill highest of VBM with an essentially persistent group at CBM of the DOS spectrum for all of the AlX (X=S, Se, and Te) sheets that are incidental group gap semiconductors. These sheets have exclusive electronic constructions with level bands at VBM and parabolic bands at CBM. AlX monolayers have no negative frequency in any phonon branches, this supports their dynamical stability of nanosheet. The AlX (X = S, Se, Te) sheets, in particular the Al-Se sheet, might be employed as prospective candidate matrices for thermoelectric nanocomposites.

A. Inamdar *et al*. in 2020 [47] investigated the activity of alkaline and pristine atoms (Na, K, and Ca) doped in a $SnSe_2$ monolayer. Modern DFT calculations were being performed to estimate the catalytic activity of the pristine and doped $SnSe_2$ using adsorption and free energy assessment of gypsum subjected to hydrogen and oxygen uptake. Their findings alleviate **demonstrated that alkaline mineral selective doping might be used to**

the drawbacks of SnSe2's poor catalytic activity at the basal level, which was previously observed.

Demirtas *et al*. in 2020 [48] were successfully designed and analyzed Al_2XX(X//X: O, S, Se, Te) sheets. Stability investigations of Al_2XX(X//X: O, S, Se, Te) tools were carried out using phonon dispersion calculations and ***ab initio*** molecular dynamic (AIMD) simulations. As a result, while Al_2TeO is dynamically unstable, Al_2SeO is also susceptible to instability at high temperatures, according to the data. The other Janus systems that have been anticipated are stable under normal conditions. They are in between the binary elements of Al_2XX, and they decrease with elongation as a result of their predicted cohesive energies. Ternary sheets are semiconductors in the same way as their binary counterparts, however, they are indirect semiconductors. It has been discovered to be particularly sensitive to strain, and as a result, it may be easily modified by applying compressive or tensile strain. As a result of the research conducted, it was discovered that stable sheets with a direct bandgap (lying) may be produced by designing Al_2XX structures, as well as systems with such characteristics.

They have the potential to be suitable materials for a wide range of optoelectronic applications.

Khosa *et al*. in 2021 [36] investigated the physical, electrical, and thermoelectrical characterises of the Janus Al_2SSe sheet were investigated using the DFT theory: They discovered that the Janus Al_2SSe monolayer is a semiconductor with an indirect bandgap of 2.03 eV which is comparable to that of silicon. The absence of imaginary phonon frequency in this Janus monolayer serves as a confirmation of the dynamic stability of the system. When proper carrier concentrations are used, it is revealed that the ideal values of ZT are 0.530 (0.190) at room temperature and 0.700 (0.480) at seven hindered K for N-type ((p-type)) Janus Al_2SSe sheets are 0.53 (0.19), at room temperature and 0.700 (0.480), at seven hindered K. Using n-type

and p-type sheets, they proved that this class of materials is high-efficiency piezoelectric semiconductors and that they may be used as potential candidates for the manufacturing of thermoelectrical electronics by mixing them with other materials.

B. Babariya *et al.* in 2021[49] proposed the modulation of the bandgap for optoelectronic applications, as well as the optical response of stacked MoX_2 (X = S, Se, Te). Through paying *ab initio* controls, they investigated the structural, phonon dispersions relations, electrical, with visual characteristics of MoX_2 (X = S, Se, and Te) since a monolayer of a quad-layer structure. In covered MoX_2 (X = S, Se, Te), the electronic band structure has a semiconductor charisma with degeneracy increasing with the numeral of sheets. A significant difference in indirect bandgap energy likened to direct bandgap energy was noticed when the number of layers decreases from quad-layer to monolayer, indicating the presence of d orbital interactions in MoX_2 (X == S, Se, Te). The refraction rises with the number of sheets and may reach values as high as 4.340, 4.110, and 4.08, respectively, and 2.050 eV at energies of 2.450 eV with 2.050 eV, respectively,

R. Ghazi *et al*. in 2021[11] investigated the transition metal dichalcogenides layer $PtS_2(Se_2)$ for its structural, electrical, and optical characteristics in preparation for nanoelectronic applications. Their theoretical investigation dealt with monolayer materials of a novel class of materials including 2D transitional metallic dichalcogenides, such as Pt S_2 (Se_2), which must distinct geometrical, physical, electrical, with visual characteristics and was investigated. According to the phonon calculations, Because of their procedure, these sheets have shown their ability to maintain their dynamical stabilities. Additionally, the direct band gaps for MoS_2 and $MoSe_2$ placed at the K point are 1.670 eV with 1.484 eV, correspondingly, while the direct band gaps for Pt-S_2 and Pt-Se_2 are

positioned in the middle of M topics are 1.8870 and 1.660 eV, correspondingly. Furthermore, an indirect bandgap of Pt-S_2 is approximately 1.775 eV at the K-M path, whereas the bandgap of Pt-Se_2 is 1.4010 eV at the K-M path.

Haman *et al.* in 2021 [30] studied the structural, electrical, and optical properties of AlX (where X = O, S, Se, and Te) using the density functional theory. In addition, the photocatalytic activities of AlX (where X = O, S, Se, and Te) have been investigated in detail. AIMD simulations and phonon dispersion carve were used to verify the updraft and dynamical stability. When the HSE06 functional is used to compute the band gaps, the findings obtained from electronic band constructions show that Al-O, Al-S, Al-Se, and Al-Te sheets are semiconductors with band gaps are equals 1.8460, 2.8870, 2.740, with 2.490 eV, respectively. The absorptional spectral of the investigated materials were analyzed, and it was observed that all AlX exhibit strong absorption n coefficients in the visible and ultraviolet wavelength ranges. Furthermore, when the estimated band-edge positions are compared to the redox potentials of water, it is discovered that the compounds have heightened photocatalytic activity and might be employed as semiconductor photocatalysts for H_2 production. It follows that the Al-O monolayer is extremely sensitive to electrical fields, making it extremely beneficial in the creation of hydrogen. Furthermore, these findings demonstrate a new route for H_2 obtained through photocatalytic H_2O utilizing Al-X sheets, which is promising.

A. Bafekry *et al.* in 2021 [50] used the first time DFT calculations to conduct a detailed analysis of the fundamental and electronic characteristics of the Bi-Te-Cl and Bi-Te-Br Janus sheets, the results were published in Science. Polycrystalline Bi-Te-Cl and Bi-Te-Br sheets have electronic bandgaps of 0.830 with 0.800 eV, respectively, and are semiconductors. The findings likewise revealed of the number of layers

increased could result in induction in the semiconductor-to-metal transition. As well as applying an electrical field to the electronic construction, mechanical uniaxial with biaxial strain is also used to investigate the modification of the electronic structure. The results reveal that the bandgaps have changed significantly and that an unintended-straight group gap transition may be generated. Theis work emphasizes the promising potential of the use of stacked sheets of Bi-Te-Cl and Bi-Te-Br of innovative electronic and energy conversational systems in electronic and energy change systems.

Haman. et. al. in 2022 [31] examined the 2D Januus aluminum Oxysullfide Al_2OS monolayer's photocatalytic performance in comparison to the parental aluminum sulfide (AlS) sheets based on the bonding energy with Giybbs allowed energies obtained done DFT calculations, as well as the photocatalytic presentation of the 2D Januus Al-Oxysulfide Al_2OS sheets. The Janus Al_2OS is a direct semiconductor with a bandgap of 2.110 eV when the HSE06 functional is utilized in the band structure investigation.

1.7 The Aims of the Study

The aim of this work focus achieve the following goals :-

1.Study of structural,optical and effect on the (Al2Br2Se2,Al2Br2S2).

2.The prediction of the suitable applications of these structures for optoelectric applications.

Chapter Two

Theoretical Part

2.1 Schrödinger Equation

Computational physics and chemistry are one of the most important goals of physics to describe the physical properties of interacting many-particle systems. Any problem can be treated in the electronic structure for any system by quantum mechanical laws, Schrödinger equation is used to describe the motions of atomic and subatomic systems, electrons, and nuclei [51]. This equation was published in 1962 by the Austrian scientist Schrödinger, the equation depends mainly on the physical situation. Therefore, the most common form is the time-dependent Schrödinger equation which describes the evolution of a system over time (t) [52].

$$\hat{H}\Psi = \hat{E}\Psi \qquad (2.1)$$

Here: Ψ Represents the wave function, $\hat{H}$ Represents the Hamiltonian operator, and E describes the system's total energy equation,

Hamiltonian operator contains kinetic ($\hat{T}$) and potential ($\hat{V}$) energy for all particles, is given by [53].

$$\hat{H} = \hat{T} + \hat{V} \qquad (2.2)$$

$$\hat{T} = \hat{T}_e + \hat{T}_n \quad , \quad \hat{V} = \hat{V}_{ne} + \hat{V}_{ee} + \hat{V}_{nn} \qquad (2.3)$$

Here: ($\hat{T}_e$): Represents the kinetic energy of the electrons ;

$\hat{T}_n$: Represents the kinetic energy of the nuclei ;

$\hat{V}_{ne}$: Represents the electrons-nuclei interaction energy;

$\hat{V}_{ee}$: It represents the interaction energy between the electrons;

$\hat{V}_{nn}$: Represent the nucleus-nucleus interaction energy.

The kinetic energy operator is given as [54].

$$\hat{T}_e = -\frac{\hbar^2}{2m_i}\sum_i \nabla_i^2 \quad (2.4)$$

$$\hat{T}_n = -\frac{\hbar^2}{2\,M_A}\sum_A \nabla_A^2 \quad (2.5)$$

where, m_i and M_A are the electron and nuclear mass, respectively.

$\nabla^2 = \frac{\partial^2}{\partial x^2} + \frac{\partial^2}{\partial y^2} + \frac{\partial^2}{\partial z^2}$ Is the Laplacian operator of (i) electrons and (A) nuclear.

The potential energy operators are given as [55].

$$\hat{V}_{ne} = -\frac{1}{4\pi\varepsilon_o}\sum_A \sum_i Z_A \frac{e^2}{r_{iA}} \quad (2.6)$$

$$\hat{V}_{ee} = \frac{1}{4\pi\varepsilon_o}\sum_{i<j}\frac{e^2}{r_{ij}} \quad (2.7)$$

$$\hat{V}_{nn} = \frac{1}{4\pi\varepsilon_o}\sum_{A<B} Z_A Z_B \frac{e^2}{R_{AB}} \quad (2.8)$$

$$\hat{H} = \hat{T} + \hat{V} = -\frac{\hbar^2}{2m}\sum_{i=1}^{n}\nabla_i^2 - \frac{\hbar^2}{2}\sum_{A=1}^{K}\frac{1}{M_A}\nabla_A^2 + V(r,R) \quad (2.9)$$

$$\hat{V} = \frac{e^2}{4\pi\varepsilon_o}\left[-\sum_{A=1}^{n}\sum_{i=1}^{K}\frac{Z_A}{r_{iA}} + \sum_{i<j}^{n}\frac{1}{r_{ij}} + \sum_{A<B}^{K}\frac{Z_A Z_B}{R_{AB}}\right] \quad (2.10)$$

where: $r_{ij} = |r_i - r_j|$ is the distance between i electron and j electron, Z_A *is* the charge of nuclei A, and Z_B is the charge of nuclei B.

$r_{iA} = |r_i - R_A|$, r_{iA} is the distance between electron i and nucleus A.

$R_{AB} = |R_A - R_B|$, R_{AB} is the distance between (A) nucleus and (B) nucleus [56].

$$\hat{H}_{Total} = -\frac{1}{2}\sum_{i=1}^{n}\nabla_i^2 - \frac{1}{2}\sum_{A=1}^{K}\frac{1}{M_A}\nabla_A^2 - \sum_{A=1}^{K}\sum_{i=1}^{n}\frac{Z_A}{r_{iA}} + \sum_{i=1}^{n-1}\sum_{j=i+1}^{n}\frac{1}{r_{ij}} + \sum_{A=1}^{K-1}\sum_{B=A+1}^{K}\frac{Z_A Z_B}{R_{AB}} \quad (2.11)$$

The total Hamiltonian equation may be written more compactly as [53],

$$\hat{H}_{Total} = \hat{T}_e + \hat{T}_n + \hat{V}_{ne} + \hat{V}_{ee} + \hat{V}_{nn} \quad (2.12)$$

To be more specific, the Schrödinger equation has an exponentially increasing complexity with the number of electrons. The solution of the Schrödinger Equation in this form is impractical. We are not able to solve this equation in general. However, this was recognized in 1929 when Dirac stated, "The underlying physical laws are known, but their application requires highly convoluted mathematics [57]. Therefore, it is essential to use approximations.

2.2 The Born-Oppenheimer Approximation

A molecule contains both nuclei and electrons, the motion of electrons and the motion of nuclear in molecules can be separate this is called the Born- approximation [58]. This approximation was published (1927) to simplify solving the Schrödinger equation and to allow chemists to calculate the theoretical energy levels of molecules, reducing them to mathematical functions they could solve. Also, this style is commonly referred to as the adiabatic approximation [59]. For Born-Oppen approximation, the nuclei are static; there is no requirement to include any

kinetic energy if nuclei are stationary. The equation to be solved is written then [59].

$$\Psi_{total} = \Psi_{electron} * \Psi_{nucleus} \quad (2.13)$$

Nuclei kinetic energy is removed and the potential energy of nuclei-nuclei could be considered fixed. In this respect, the nuclei kinetic energy and the potential energy of nuclei-nuclei can be removed from the Hamiltonian operator and the Hamiltonian operator $\hat{H}$ is simplified as the following[60],

$$\hat{H} = \hat{T}_e + \hat{V}_{ne} + \hat{V}_{ee} \quad (2.14)$$

The system can be described as all electrons moving in a potential field of nuclei with fixed positions. Therefore, the total energy calculation of a molecule is much simplified and computations of wave functions of the large molecule could be solved [61].

2.3 The Hartree - Fock Approximation

As known, solving the Schrödinger equation for all electrons in systems requires solving many simultaneous differential equations [62]. The calculations are very difficult and need to simplify the methods and the problem itself. In 1928**.** In a first attempt, Hartree proposed an approximate solution to it. The Hartree approximation consists in considering the electrons as independent, and that the rest of the electrons will produce an average field that allows the independent electrons to evolve through it. This approximation reduces the electron problem in interaction with the problem of the singular electron method. The Hamiltonian may be as a sum of (n) Hamiltonians, representing a single electron behavior for each [63].

$$E_{\Phi} = \frac{\langle \Phi | \hat{H} | \Phi \rangle}{\langle \Phi | \Phi \rangle} \geq E_0 \qquad (2.15)$$

Here, E_0 is the ground-state energy. Using this theory, the perfect ground-state wave function is approximated from the experiment function that produces the lowest energy. Hartree found the Hamiltonian equation of the many-electron system and each electron can be separately processed as a single particle. The wave function of the Hartree-Fock approach can be written in a determinant called the Slater determinant. This determinant makes two considerations: the first is the spin of all electrons, and the second is the Pauli exclusion principle. (α) represents the spin-up of electrons, and (β) represents spin-down of electrons. For the N-electron system, we can write the Slater determinant in the following form.

$$\Psi = \frac{1}{\sqrt{N!}} \begin{vmatrix} \Psi_1(1)\alpha(1) & \Psi_1(1)\beta(1) & \Psi_2(1)\alpha(1) & \Psi_2(1)\beta(1) & \dots & \Psi_N(1)\alpha(1) & \Psi_N(1)\beta(1) \\ \Psi_1(2)\alpha(2) & \Psi_1(2)\beta(2) & \Psi_2(2)\alpha(2) & \Psi_2(2)\beta(2) & \dots & \Psi_N(2)\alpha(2) & \Psi_N(2)\beta(2) \\ \vdots & & \vdots & & & \vdots & \\ \Psi_1(N)\alpha(N) & \Psi_1(N)\beta(N) & \Psi_2(N)\alpha(N) & \Psi_2(N)\beta(N) & \dots & \Psi_N(N)\alpha(N) & \Psi_N(N)\beta(N) \end{vmatrix} \qquad (2.16)$$

Here: Ψ represents the electronic wave function, α describes the spin-up of electrons and β describes the spin-down of electrons, respectively, and the normalization factor is $\frac{1}{\sqrt{N!}}$. For Hartree-Fock methods, the main step is to first introduce the molecular orbital expansion and secondly determine the corresponding coefficients based on the covariance principle [58]. The molecular orbitals $\Psi_i(r)$ the Hartree-Fock equation was solved by the iterative process of the Self-Consistent-Field (SCF) producer yields [64].

$$\hat{F}\Psi_i(\vec{r}) = \varepsilon_i \Psi_i(\vec{r}) \qquad (2.17)$$

Here, ε_i is the electronic energy of the electron in the orbital, and F represents the Fock operator. For closed-shell systems,

$$\hat{F} = \hat{h} + \sum_{l=1}^{n/2} (2J_l - K_l) \qquad (2.18)$$

With, J_l and K_l are the Coulomb operator and the exchange operator, respectively,

$$J_l\Psi(\vec{r}) = \int \frac{\Psi_l^*(\vec{r})\Psi_l(\overrightarrow{r'})}{\left|\vec{r} - \overrightarrow{r'}\right|} dV'\Psi(\vec{r}) \qquad (2.19)$$

$$K_l\Psi(\vec{r}) = \int \frac{\Psi_l^*(\vec{r})\Psi_j(\overrightarrow{r'})}{\left|\vec{r} - \overrightarrow{r'}\right|} dV'\Psi(\vec{r}) \qquad (2.20)$$

This correction takes into calculation the effects of spin correlation. First: (MO) represents the final expansion correction of the molecular orbital, and secondly: (LCAO) represents the linear atomic orbital structure [62]. Thus an Ψ_i is defined as molecular individual orbital.

$$\Psi_i(x) = \sum_{\mu=1}^{N} C_{\mu i}\Phi_\mu(x) \qquad \mu = 1,2,\dots,N \qquad (2.21)$$

The basis functions Φ_μ are selected to be normalized, N number of the basis functions, and $C_{\mu i}$ represents the molecular orbital expansion coefficients. An appropriate set of orbital expansion fundamental functions must be chosen so that we can then adjust for two factors (C μi) to reduce the calculated total electronic energy of the multi-electron wavefunction. The value of the resulting energy in the chosen constraints will be as close as possible to the exact energy E_0 of the ground state system [65].

$$E(\Phi_1, \Phi_2, \dots\dots, \Phi_N) \geq E_0 \qquad (2.22)$$

Ψ is the exact ground state function, and the equal sign is only applied in this state.

2.4 Density Functional Theory (DFT)

Density functional theory (DFT) is a method used to calculate the electronic composition of solids, molecules, and atoms, and it is one of the most popular, powerful, versatile, and successful quantum mechanical modelling methods. The properties of the multiple electron system can be determined in this theory using functions, which depend on the electron density distribution in this case $ƒ(\vec{r})$, this density functions [66]. The electronic system energy may be calculated using the electronic density function by these two properties: $ƒ(r\rightarrow\infty) = 0$; $\int ƒ(r)\, dr = n$

It represents the possibility of finding an electron in a unit volume centered around a position. On the road to explaining the system, it seems to contain enough information, although there is more information, some of it is not required. Therefore, Electron density is necessary for the atomic structure to fully determine its properties.

2.4.1 Hohenberg –Kohn Theorem

In 1964, Hohenberg and Kohn formulated the fundament for DFT with the central idea to substitute many-body problems with an equation for the electron density $n(\vec{r})$.

The Hamilton operator of the n-electron system within the Born-Oppenheimer approximation can be written by [58],

$$\hat{H} = \hat{T} + \hat{V}_{ext} + \hat{V}_{ee} \qquad (2.23)$$

The external potential $\hat{V}_{ext}$ is uniquely defined by the electron density $\rho(\vec{r})$. The total energy can be written as [67].

$$E_0 = T[\rho_0] + \int V_{ext}(r)\rho_0(r)dr[\rho_0] + J[\rho_0] + E_{NC} \qquad (2.24)$$

where $T[\rho_0]$ Describe kinetic energy, $E_{NC}[\rho_0]$ Represents the interaction energy between an electron and a non-classical electron and $J[\rho_0]$ is the classical Coulomb energy defined as,

$$J[\rho_0] = \frac{1}{2}\iint \frac{\rho_0(r_1)\rho_0(r_2)}{|r_1 - r_2|} dr_1 dr_2 \qquad (2.25)$$

$V_{ext}(r)$ directly depends on the system, which is the Coulomb potential of the nuclei. Thus, the total energy can be written as,

$$E_0 = \int V_{ext}(r)\rho_0(r)dr + F_{HK}[\rho_0] \qquad (2.26)$$

Here: F_{HK} is a global function to describe electron density,

$$F_{HK}[\rho] = J[\rho] + T[\rho] + E_{NC}[\rho] \qquad (2.27)$$

HK theory assumes that F_{HK} exists, but the real form of F_{HK} is not known and must be approximated. HK theorem reduced the problem of solving the Schrödinger equation for many bodies to the problem of reducing functional density [68].

2.4.2 The Kohn-Sham Theory

There exists an unreactive system in the real system with the ground state density ρ(r) with the same ρ(r). Equation (2.27) can rewrite as:

$$F[\rho] = T_S[\rho] + J[\rho] + E_{NC}[\rho] \qquad (2.28)$$

Where $T_S[\rho]$ is the Kinetic energy of the noninteracting electron system. The electron density of the noninteracting system is described by a single Slater determinant of orbitals.

The DFT exchange-correlation energy $E_{xc}[\rho]$ of interacting electron system can be defined in the form:

$$E_{xc}[\rho] = T[\rho] - T_S[\rho] + E_{NC}[\rho] \quad (2.29)$$

By applying the variation precept, $\delta E/\delta\rho(r)=0$, Kohn–Sham for functional:

$$E[\rho] = \int \rho_{(r)}\, v_{(r)} dr + T_S[\rho] + J[\rho] + E_{xc}[\rho] \quad (2.30)$$

The density $\rho(r)$is given by:

$$\rho(r) = \sum_{i=1}^{n} \left| \phi_i (r) \right|^2 \quad (2.31)$$

This results in one–electron in the Hartree-type of equations:

$$\left[-\frac{1}{2}\nabla^2 + V_{(r)} + \int \frac{\rho(r)}{\left| r - \bar{r} \right|} d\bar{r} + V_{xc}(r) \right] \phi_i(r) = \varepsilon_i \phi_i(r) \quad (2.32)$$

Where, $V_{xc}(r)$ is the exchange-correlation potential, $\phi_i(r)$ is Kohn–Sham orbitals, and ε_i is Kohn –Sham orbital energies:

$$V_{xc}(r) = \frac{\delta E_{xc}[\rho]}{\delta \rho_{(r)}} \quad (2.33)$$

Equations (2.31) – (2.33) contain one unknown term and are very accurate and are known as the Kohn -Sham equations, $E_{xc}[\rho]$. Kohn–Sham's approach is a famous work that was embraced for many purposes [69].

2.4.3 Exchange-Correlation Energy

Correlation is a term used to describe interactions between electrons in the same molecule. The basis of the density functional theory of Kohn Hohenberg, and Sham is that sum of the binding energies of an ordinary electron gas and its exchange energies can be calculated by knowing its density. [70] The Kohn-Sham exchange and correlation functional are [71].

$$E_{xc}[\rho] = T[\rho] - T_S[\rho] + V_{ee}[\rho] - J[\rho] \quad (2.34)$$

Here, $T_S[\rho]$ The kinetic energy of the non-interacting system.

When the Hamilton factor is multiplied by the scaling factor λ, and when λ = 0 we get a system of non-interacting electrons system of non-interacting, while for λ=1, a system of fully interacting electrons will be obtained. From Hohenberg –Kohn theorem, the non-interactive ρ can be obtained.

$$F_{\lambda=1}[\rho] = F[\rho] = T[\rho] + V_{ee}[\rho] \quad (2.35)$$

$$F_{\lambda=0}[\rho] = T_s[\rho] \quad (2.36)$$

Thus, equation (2.34) will be,

$$E_{xc}[\rho] = F_{\lambda=1}[\rho] - F_{\lambda=0}[\rho] - J[\rho] \quad (2.37)$$

$$E_{xc}[\rho] = \int_0^1 d\lambda \frac{\partial F_\lambda[\rho]}{\partial \lambda} - J[\rho] \quad (2.38)$$

Using Hellmann – Feynman theorem [70] :

$$\frac{\partial F_\lambda[\rho]}{\partial \lambda} = < \varphi^\lambda \left| V_{ee} \right| \varphi^\lambda > \quad (2.39)$$

Where, φ^λ represents the wave function to the Hamilton operator. Equation (2.38) will be,

$$E_{xc}[\rho] = \int_0^1 d\lambda < \varphi^\lambda \left| V_{ee} \right| \varphi^\lambda > - J[\rho] \quad (2.40)$$

$$E_{xc}[\rho] = \frac{1}{2} \iint \frac{1}{r_{12}} \rho(r_1) \bar{\rho}_{xc}(r_1, r_2) dr_1 dr_2 \quad (2.41)$$

$\bar{\rho}_{xc}$ defined is the averaged exchange-correlation [15] :

$$\bar{\rho}_{xc}(r_1, r_2) = \rho(r_2) \bar{h}(r_1, r_2) \quad (2.42)$$

Here, $\bar{h}(r_1, r_2)$ Describes the pair averaged binding function.

$$\int_0^1 d\lambda\, \rho^{\frac{\lambda}{2}}(r_1, r_2) = \frac{1}{2}\rho(r_1)\rho(r_2)\left[1 + \bar{h}(r_1, r_2)\right] \quad (2.43)$$

Here: $\rho^{\frac{\lambda}{2}}(r_1, r_2)$ is the diametrical component from a matrix of two-particle densities. The energy of interchange-correlation relies upon only a spherically average $\bar{\rho}_{xc}(r_1, r_2)$,

$$E_{xc}[\rho] = \frac{1}{2}\int dr\, \rho(r) \int_0^\infty 4\pi s ds \rho_{xc}^{SA}(r, s) \quad (2.44)$$

Here,

$$\rho_{xc}^{SA}(r, s) = \frac{1}{4\pi}\int \bar{\rho}_{xc}(r, \bar{r}) d\bar{r} \quad (2.45)$$

From the Kohn–Sham density functional theory, the exchange-correlation functional E_{xc} is detached into the correlation E_c^{ks} parts then the exchange E_x^{ks},

$$E_{xc}[\rho] = E_x^{ks}[\rho] + E_c^{ks}[\rho] \quad (2.46)$$

Where, $E_c^{ks}$is Represents the calculation of the Hartree-Fock exchange energy with Cohen Sham Φ_ρ

$$E_x^{ks}[\rho] = < \phi_\rho \left| \hat{V}_{ee} \right| \phi_\rho > - J[\rho] \quad (2.47)$$

$$E_c^{ks}[\rho] = < \Psi_\rho \left| \hat{V}_{ee} \right| \Psi_\rho > - < \phi_\rho \left| \hat{V}_{ee} \right| \phi_\rho > \quad (2.48)$$

Here, Ψ_ρ is the exact interacting wavefunction.

2.5 The Local (Spin) Density Approximation (L(S) DA):

The oldest, simplest, and possibly the most important function is the local density approximation (LDA), Presented by Hohenberg and Kohn in their original paper DFT [72]. LDA is the simplest approximation of E_{XC} [ρ(r)], which assumes that the system is a homogeneous electronic gas and that E_{XC} [ρ(r)] depends only on the local value of the electron density. Therefore, E_{XC}[ρ(r)] can be written in a simple form [73].

$$E_{xc}^{LDA}[\rho] = \int \rho(\vec{r})\varepsilon_{xc}\left(\rho(\vec{r})\right)d\vec{r} \qquad (2.49)$$

Here: ε_{xc} Representexchange-correlation energy of each particle. Compared to LDA, LSDA defines the exchange-correlation potential in terms of the density of α and β spins (i.e. spin up and spin down respectively) and was developed for calculating the properties of open-shell systems [8]

$$E_{xc}^{LSDA}[\rho_\alpha, \rho_\beta] = \int \rho(\vec{r})\varepsilon_{xc}\left(\rho(\vec{r})_\alpha, \rho(\vec{r})_\beta\right)d\vec{r} \qquad (2.50)$$

For certain properties such as equilibrium structures, vibrational frequencies, and dipole moments, the LSD approximation provides better results than HF; however, it cannot determine the highly precise energy details as many analytical chemists wish. Overall, LSDA provides useful information on those systems that are very similar to regular electron gas, i.e. those in which the density slowly varies with mode. However, in reality, atomic and molecular systems do not have a uniform electron density and therefore need more complex models.

2.6 The General Gradient Approximation (GGA).

To create a very precise approximation of the cross-link energy, it includes the color gamut of the electron density as well as the electron density functions [5]

$$E_{xc}^{GGA}[\rho_\alpha, \rho_\beta] = \int f\left(\rho_\alpha, \rho_\beta, \nabla_{\rho_\alpha}, \nabla_{\rho_\beta}\right) d\vec{r} \qquad (2.52)$$

These functions provide a general development for LSDA as they explain the contrast of severity with the position. E_{xc} is usually written as a combination of the terms Exchange (E_x) and Correlation (E_c) to simplify the problem.

$$E_{xc} = E_x + E_c \qquad (2.53)$$

Then instead of HF orbitals and the approximate solutions of Ec, the energy exchange function can be obtained from the exchange term HF with Kohn-Sham orbitals. Another functionals of exchange then link has been developed independently then can be combined in different ways. One popular functional of GGA functions is PBE, Perdew, Burke, and Enzerhof (PBE) [78].

2.7 The Hybrid Functional

Hybrid functions are a functional class of interchange-correlation energy functional approximations called DFT and combine part of precise interchange from HF notion for interchange and correlation from different sources :(empirical or initio). Instead of density, the exact exchange energy function is expressed in terms of Kohn-Sham orbitals, so express it implicit density functional. Often cross-link function is constructed as a linear set of

the HF micro-crossover function (E_x^{HF}) and any number of explicit cross-link and cross-link functions [75].

One GGA functional is known as the PBE functional, abbreviated as the PBE functional. PBE came up with enhancement factors for both the exchange energy and the correlation energy. The correlation term for PBE is given by,

$$E_{xc}^{hybrid} = E_{xc}^{GGA} + a(E_x^{HF} - E_x^{GGA}) \quad (2.51)$$

Here: Based on the foundations of perturbation theory, (a is equal to 1/4) [76] It performs for a class of functions with just as many parameters as the latent GGAs.

2.8 Perdew, Burke, and Ernzerhof (PBE)

The GGA functions have many varied examples, such as GGA proposed by PBE. The exchange part is given by [77].

$$\epsilon_x^{PBE} = \epsilon_x^{HEG} F_x^{PBE} \quad (2.54)$$

$$F_x^{PBE} = 1 + K - \frac{K}{1+\left(\frac{\mu s^2}{K}\right)} \quad (2.55)$$

Here, K = 0.804 ,μ = 0.21951. While the linked part is selected as,

$$\epsilon_{xc}^{GGA} = \epsilon_c^{HEG} + H(r_s, \zeta, t) \quad (2.56)$$

Here: $(n^{\downarrow} - n^{\uparrow})$ /n, Represents the spin polarization, While the local value of the density factor is r_s, then $t = |\nabla_n| / (2\phi K_{TF^n})$ Represents dimensionless gradient, now $\phi = [(1+\zeta)^{\frac{3}{2}} + (1-\zeta)^{\frac{3}{2}}]/2$ finally H by giving [77],

$$H = \frac{e^2 \gamma \phi^3}{a_\circ} \log(1 + \frac{\beta t^2}{\gamma} \frac{1 + At^2}{1 + At^2 + A^2 t^4}) \quad (2.57)$$

Function A represents

$$A = \frac{\beta}{\gamma}\left[e^{\frac{-a_\circ\, \epsilon_X^{HEG}}{e^2\, \gamma\, \phi^3}} - 1\right]^{-1} \qquad (2.58)$$

2.9. Plane Wave Pseudo-Potential method (PW-PP)

The efficiency of DFT calculations is expected to be based primarily on the efficiency of the Pseudo-Potential Plane Wave (PP-PW) method. In this section, we will try to clarify Bloch's theory and the pseudo-potential approach.

Bloch's theory states that the electronic wave function is a combination of a periodic component of a cell and a wave component of a periodic solid [79].

$$\Psi_i(\vec{r}) = f_i(\vec{r})\, \exp\left[i\vec{k}.\vec{r}\right] \qquad (2.59)$$

$$f_i(\vec{r}) = f_i\left(\vec{R} + \vec{r}\right) \qquad (2.60)$$

Here: $\vec{k}$ Represents a vector of a mutual space confined to the first Brillouin region, i Represent the band index and $\vec{R}$ Represents a vector of direct lattice i.e. Bravais lattice. A discrete set of plane waves is contained in the wave function cell-periodic component with reciprocal crystal lattice vectors.

$$f_i(\vec{r}) = \sum_G C_{i,G}\ \exp\left[i\vec{G}.\vec{r}\right] \qquad (2.61)$$

Here: the reciprocal lattice vectors $\vec{G}$ are defined by;

$\vec{G}.\vec{R} = 2\pi m;$ for all $\vec{R};$ where $\vec{R}$ Represent lattice vector of crystal, also m is an integer. This leads to writing the function electronically as a sum of the plane waves

$$\Psi_i(\vec{r}) = \sum_G C_{i,K+G}\ \exp\left[i(\vec{k} + \vec{G})\right].\vec{r} \qquad (2.62)$$

Infinite numbers of k points are located in the the1^{st} Brillouin zone and their basis of operation require infinite plane waves that are set to completely reconstruct the system by symmetry. The first Brillouin zone was sampled in specific groups of k points to overcome the problem of calculations in that pattern. To apply the calculations, several sampling methods for the Brillouin zone are proposed.

2.10 CASTEP Code

CASTEP (Cambridge Sequential Total Energy Package) is a quantum mechanical program for beginners that uses (DFT) density functional theory to simulate properties of liquids, solids, structures, also textures with a broad variety of types of materials for example metals, ceramics, and semiconductors. In principle, the calculations allow researchers to investigate the origin as well as the nature of the optical, structural, and electronic properties of the system without empirical input. CASTEP is an ideal simulation method for researching problems in chemical engineering, solid-state physics, materials, and molecular sciences where experimental models and experimental data are lacking. With the assistance of CASTEP, researchers can save a lot of time and costly trials. CASTEP can calculate many optical, electronic and magnetic, elastic constants and other physical properties. Specifically, it can also foresee electronic properties such as Schottky barriers, band gaps, and; Optical properties such as dielectric functions, absorption, reflectivity, infrared, and spectra. To minimize the computation complexity, The core electrons were replaced by valence electrons, which operate at the active potential of the system. Electronic wave functions were expanded through a plane-wave base set, also generalized gradient (GGA) approximations or local density (LDA) was used to calculate the electrons' interaction, interchange, also correlation effects in the system. Sets the structural modifications of liquids, solids,

surfaces, and interfaces are efficient due to the use of pseudopotentials and plane wave base [80].

2.11 Computational Details

In this study, we were able to research the physical, computational and electronic properties of $Al_2Br_2X_2$ When (X=S, Se) structures by using the CASTEP program's Density Functional Theory (DFT) with generalized approximations of the gradient. The precise formalism of Perdew-Burke Ernzerhof (PBE) [80,81] is used in accounts to modify electronic exchange link interactions. In this study, the model designed to simulate the monolayers of $Al_2Br_2S_2(Se)_2$ consists of (4×4×1) supercell. The constants and atomic positions of the lattice were just relaxed before an energy equilibrium of (5×10^{-6} eV/atom) reached cutting of kinetic energy, k-grid, and vacuum are reached while the overall energy variation between the dual constructive is less than (0.000001 eV). For each measurement, the energy cutoff equivalent to 510 eV was taken. For the electronic, density of state, and optical properties, the Monkhorst–Pack k-points net of (14×14×1), (26×26×1), (34×34×1), grid were used respectively. To prevent interactions with neighboring layers, avoid spacing was set (27 Å) along the z-direction.

A complex dielectric function consists of summing up the real and the imaginary parts as follows.

$$\varepsilon(\omega) = \varepsilon_1(\omega) + i\varepsilon_2(\omega) \qquad (2.63)$$

Where the real part $\varepsilon_1(\omega)$ and imaginary part $\varepsilon_2(\omega)$ are given by the well-known relations

$$\varepsilon_1(\omega) = 1 + \frac{2}{\pi} P \int_0^{\infty} \frac{\omega' \varepsilon_2(\omega')}{\omega'^2 - \omega^2} d\omega' \qquad (2.64)$$

$$\varepsilon_2(\omega) = \frac{e^2\hbar}{\pi m^2\omega^2}\sum_{v,c}\int_{BZ}|\langle u_{cv}|u.\nabla|u_{ck}\rangle|^2\,\delta[\omega_{cv}(k)-\omega]d^3k \qquad (2.65)$$

where: P stands for the fundamental integrative value, m electron mass, e electron charge, u unit vector, and c for matrix elements from transitions to conduction band states $u_ck(r)$ from valence band states ($u_vk(r)$). In addition, the complex refractive index containing the real part is called the refractive index (n), and the imaginary part is also called the extinction index (k) as follows:

$$n^*(\omega) = n(\omega) + ik(\omega) \qquad (2.66)$$

$$n(\omega) = \left[\frac{\varepsilon_1(\omega)}{2} + \frac{\sqrt{\varepsilon_1^2(\omega)+\varepsilon_2^2(\omega)}}{2}\right]^{\frac{1}{2}} \qquad (2.67)$$

$$k(\omega) = \left[\frac{\sqrt{\varepsilon_1^2(\omega)+\varepsilon_2^2(\omega)}}{2} - \frac{\varepsilon_1(\omega)}{2}\right]^{\frac{1}{2}} \qquad (2.68)$$

The conductivity depends on the imaginary part of the dielectric function. Also, the absorption coefficient is related to the complex refraction index according to the following equation:

$$\sigma(\omega) = \frac{\omega}{4\pi}.\varepsilon_2(\omega) \qquad (2.69)$$

$$\alpha(\omega) = \frac{2\omega}{c}.k \qquad (2.70)$$

where: c is the speed of light in a vacuum. Also, by studying the natural occurrence at the level, the reflectivity can be obtained and the energy loss function of the material represents the energy lost by the electrons passing through the material, these quantities can be given according to the following equations [82].

$$R(\omega) = \frac{(n(\omega)-1)^2 + k^2(\omega)}{(n(\omega)+1)^2 + k^2(\omega)} \qquad (2.71)$$

$$L(\omega) = \frac{\varepsilon_2(\omega)}{{\varepsilon_1}^2(\omega) + {\varepsilon_2}^2(\omega)} \qquad (2.72)$$

Chapter Three

Results and discussions

3.1 AlBrSe monolayer

The structural, electronic, and optical properties of the orthorhombic 2D AlBrSe (or $Al_2Br_2Se_2$) monolayer under the effect of strain are examined using the density functional theory (DFT) calculations. Atoms in a monolayer are linked by strong covalent bonds, Br atoms are distributed on both sides of the monolayer from the top and bottom of the layers while the Al and Se atoms are in the middle of the layer and are distributed coordinately.

3.1.1 Structural and electronic properties

Monolayer AlBrSe is a compound consisting of Al, Br, and Se atoms arranged in an orthorhombic lattice with space group Pmmn (D2h-13, No. 59). Fig.(3.1) illustrates the side and top views of the AlBrSe monolayer after the total relaxation. The calculated lattice constants of the AlBrSe monolayer are 3.585 Å (*a*) and 5.134 Å (*b*). The calculations show that the bonds lengths of the Al-Br, Al-Se1 and Al-Se2 are 2.539 Å, 2.504 Å, and 2.583 Å, respectively, which are close to each other with a very small difference, and the same thing applies to the angles θ_1 (91.435°), θ_2 (89.806°), θ_3 (89.379°), and θ_4 (85.574°) between the three atoms that make up this monolayer, even though the angle $\theta_1(\theta_{Al\text{-}Br\text{-}Al})$ is greater than the other two angles as shown in Fig.(3.1). From the above, we can see that the lattice constant (b) is about one and a half times greater than the value of the lattice constant (*a*), and this in turn leads to a difference in properties in both directions, as the difference is large and this system cannot be treated as an isotropic system like the hexagonal system. Rather, it is an orthorhombic lattice system with an anisotropic system, and this can be seen by the k-point path in the figures related to the band structure, so its properties depend on the direction. Hence, these calcultionso lead to the

conclusion that the AlBrSe monolayer could be employed in the progress of anisotropic devices. The electron localization function AlBrSe is depicted in Fig. (3.1)(a), where delocalized (0.5) and fully localized (0.9) electrons are denoted by green and red areas, respectively, while the blue region (0.0) denotes very low electron density. The red zone is largely focused on the Br and Se atoms, indicating that electrons are strongly localized around these atoms. Meanwhile, a significant spread of delocalized electrons can be seen in the green areas connecting the Br atoms to Al atoms and very low electron density in the blue areas connecting the Al atoms to Se atoms. The computed phonon dispersion curve is shown in Fig. (3.2) (a), where there is no imaginary mode of the acoustic and optical branch in either path, which is indicative of the dynamic stability of the AlBrSe monolayer. The values of the frequencies are approximately between 0 (at point Γ) and 390.94 cm^{-1} (at point X), respectively.

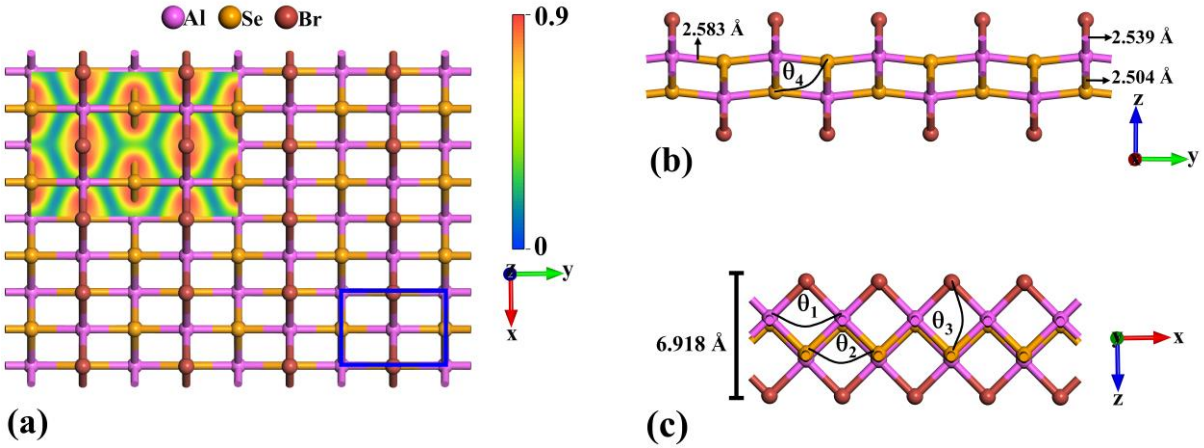

Fig. (3.1) (a) Top and (b,c) side views of the optimized structure of the AlBrSe monolayer. The snapshot in (a) refers to the electron localization function. The blue rectangle indicates the unit cell.

Moreover, AIMD is carried out to determine the thermodynamic stabilities of the AlBrSe monolayer, as illustrated in Fig. (3.2) (b), negligible

fluctuations in the total energies of this monolayer are detected, without bond breakage, distortion, or structural reconstructions, confirming their strong thermodynamic stabilities at a temperature of 300 K.

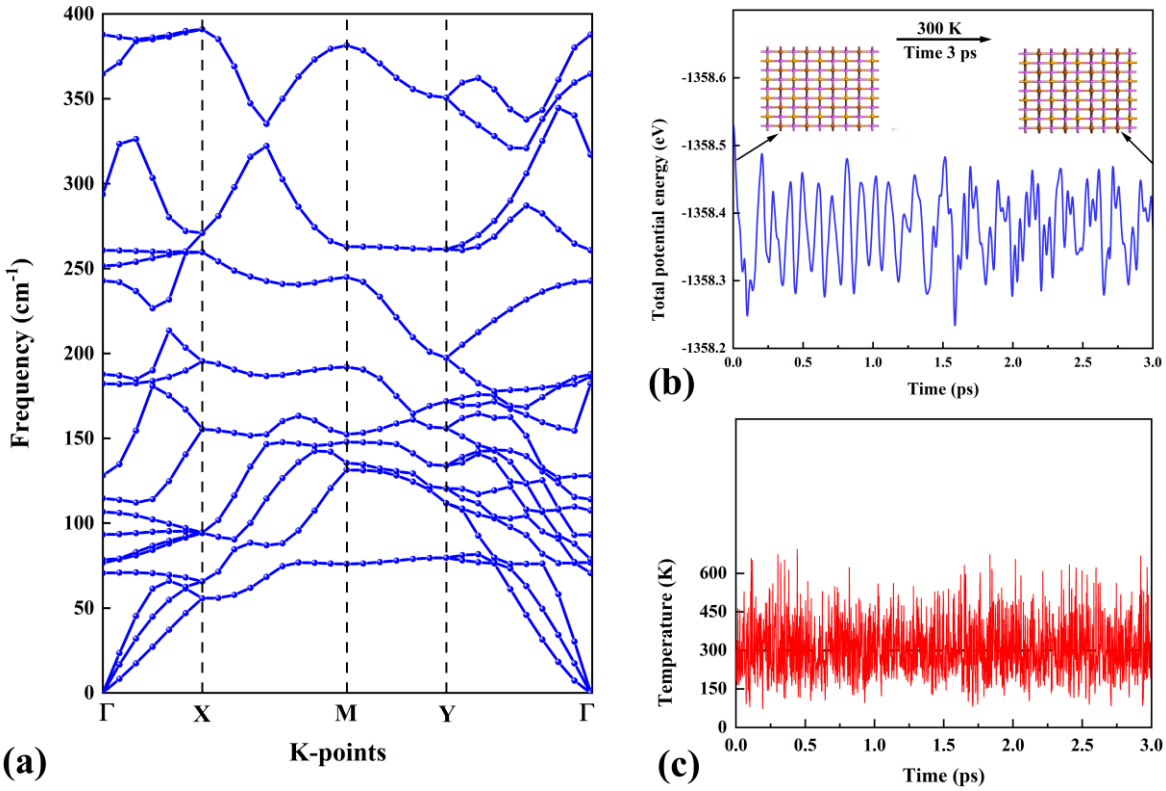

Fig.(3.2). (a) The phonon dispersion curve, (b) total potential energy as a function of time variation and (c) temperature as a function of AIMD steps at 300 K of AlBrSe monolayer.

The anticipated band structure of the AlBrSe monolayer along the high symmetric pathway Γ-X-M-Y- Γ employing the PBE and HSE06 calculations and the corresponding results are depicted in are shown in Fig. (3.3) (a). The measured electronic band structures using the PBE method appear to be extremely like the HSE06 functional, in which the valence band maximum (VBM) lies at the Γ point and the conduction band minimum (CBM) is located between the Y-Γ path, as a result, the AlBrSe

monolayer is indirect bandgap semiconductor. The calculated bandgap using the PBE approach is 1.654 eV. Nevertheless, the energy gap of a semiconductor is well known to be underestimated when using the PBE functional. The gaps calculated using the PBE functional for monolayer in this study are lower than those computed with the HSE06 method (2.231 eV). Because electronic states at the Fermi level are important in electronic transports, the partial density of states (PDOS) of each element has been determined in detail, as shown in Fig. (3.3) (b). The valence band near the Fermi level is primarily determined by the contribution of all p orbitals of the Al, Br, and Se atoms, with the emphasis that the contribution of the Br and Se atoms is much higher than the contribution of Al because of the large atomic numbers of Br and Se elements relative to the atomic number of Al, noting that there is no contribution for the s orbital in the valence band except for the contribution of the 3s orbital of the Al atom in the region beyond 4 eV. Conversely, in the conduction bands near the Fermi level, there is an empty electronic state, after that, in the region beyond about 2 eV, the conduction band is equally composed of p orbital of Al, Br, and Se atoms with a clear and distinct contribution of 3s orbital of the Al atom. One can notice that the total partial density of states consists of the sum of the contributions that were mentioned above. Based on the foregoing, the results of DOS agree with the electronic band structure.

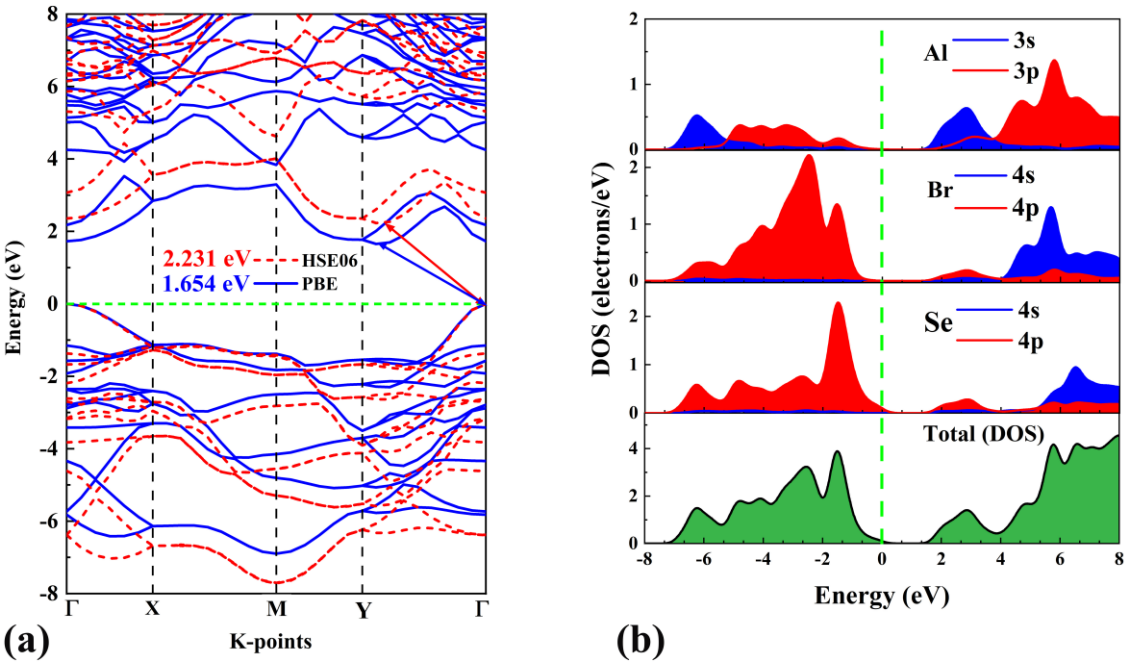

Fig.(3.3). (a) The calculated band structure by PBE and HSE06 methods and (b) partial and total density of state of AlBrSe monolayer. The green dashed line indicates the Fermi level, which is set to zero energy.

3.1.2 Photocatalytic water-splitting

The electronegativity (χ) and the positions of the energy edges of the conduction (E_{CB}) and valence bands (E_{VB}) were estimated using the following equations [83,84]:

$$\chi = \left[\chi(Al)^a * \chi(Br)^b * \chi(Se)^c\right]^{\frac{1}{a+b+c}} \quad (3.1)$$

$$E_{CB} = \chi - E_e - 0.5E_g \quad (3.2)$$

$$E_{VB} = \chi - E_e + 0.5E_g \quad (3.3)$$

Where χ is the absolute electronegativity of the AlBrSe monolayer (5.246 eV), and (a, b, and c) represented the number of atoms of an element in the monolayer, E_g is the indirect bandgap according to the HSE06 method and E_e=4.44 eV is the absolute vacuum scale for normal hydrogen electrode

[85]. The photocatalyst energy bandgap employed for water splitting must be equal to or greater than 1.23 eV. Furthermore, to split the water, the E_{CB} should be higher than the standard redox potential (H^+/H_2= -4.44 eV) and the E_{VB} lower than the oxidation potential (H_2O/O_2= -5.67 eV). As shown in Fig. (3.4) (a), the positions of the band edge were aligned with the vacuum level adjustments and were compared to the redox and the redox potentials. The energy gap of the AlBrSe monolayer (2.231 eV) is greater than 1.23 V and the edge positions of E_{CB} and E_{VB} are -4.131 eV and -6.362 eV, respectively. As a result, E_{VB} is smaller than the oxidation potential (H_2O/O_2), therefore, the photogenerated holes oxidize the water (H_2O) to form O_2. The E_{CB} of the AlBrSe monolayer, on the other hand, is higher than the redox potential (H^+/H_2). Thus, photogenerated electrons result in the reduction of produced H^+ to H_2. Based on these results, this monolayer achieves the photocatalytic conditions for water-splitting. The indirect bandgap of monolayer gives the excitons a longer average life, which in turn increases their efficiency in generating hydrogen gas, depending on the energy of solar light or from illumination by artificial sources. A similar phenomenon is also found in many monolayers [86–90] and heterostructure layers [91–94].

We estimated the work function (W) of the AlBrSe monolayer to be 5.454 eV, based on the difference between the vacuum level (E_{vac}) and the Fermi level (E_F) as depicted in Fig.(3.4) (b). Our computed work function is slightly higher than that in graphene (4.89–5.16 eV) [95]. The W on the two sides of the AlBrSe monolayer is identical because of the vertical symmetrical arrangement. Furthermore, the identical in the vacuum level leads to the identical in the photocatalytic performance at the AlBrSe two similar surfaces.

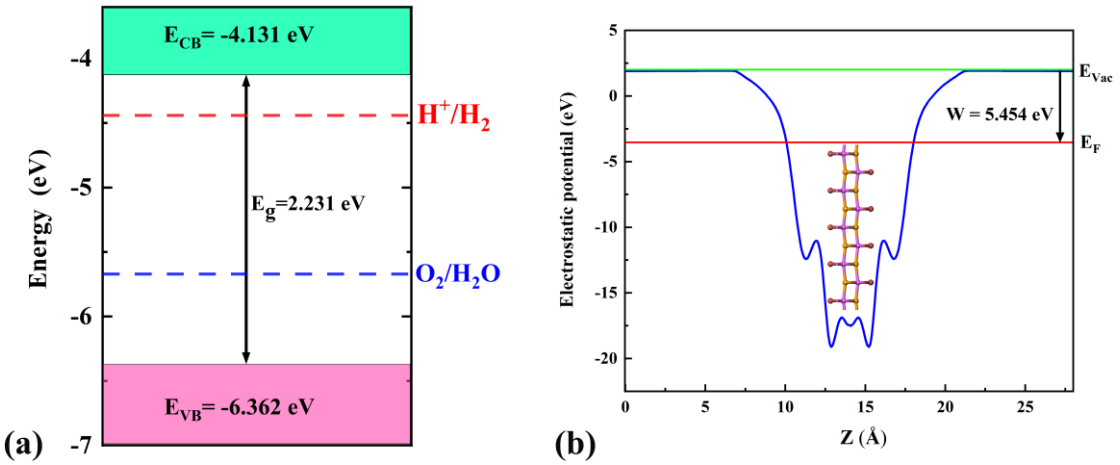

Fig.(3.4). (a) The band-edge potential and (b) The work function along the z-axis of the AlBrSe monolayer.

3.1.3 Strain effect on the AlBrSe Monolayer

Biaxial strain engineering is among the most efficacious methods of improving the electronic properties of a variety of 2D materials by modifying the band structure [96]. In our current computations, we examine the in-plane biaxial strain (δ) as $\delta = (a-a_0)/a_0 \times 100\%$, where a and a_0 are respectively the strained and unstrained lattice constants. Previous studies have demonstrated that 2D materials can tolerate high stresses ranging from -20% to 20% [97–100]. Notwithstanding this, our analysis in this research centered on a strain range of -6 to 6% based on the stability of this monolayer. The energy gaps, DOS, band-edge potential, and optical properties were investigated under the influence of tensile and compressive strains on the monolayer. As shown in Fig. (3.5), the band structures of the AlBrSe monolayer change in a coordinated manner with strain, the VBM remains centered in the unstrained state at the Γ point and the CBM is in the path Γ-Y point in the strain range between -6% to 2%, afterwards, especially at the tensile strain of 4% and 6%, the CBM has transferred to point Γ, as a result, both VBM and CBM lie at Γ point. Interestingly, this

led to a dramatic transformation in bandgaps from an indirect to direct bandgap at these two strains. However, the energy gap increases with the tensile strains, while it decreases with the compressive strain, and it is noted that the changes in the tensile strains are larger than those in the compression strain situations, where the decrease in the energy gap is greater than the increase in the case of tensile strain, decrease from 2.353 eV (at 4%) to 1.837 eV (at -6%).

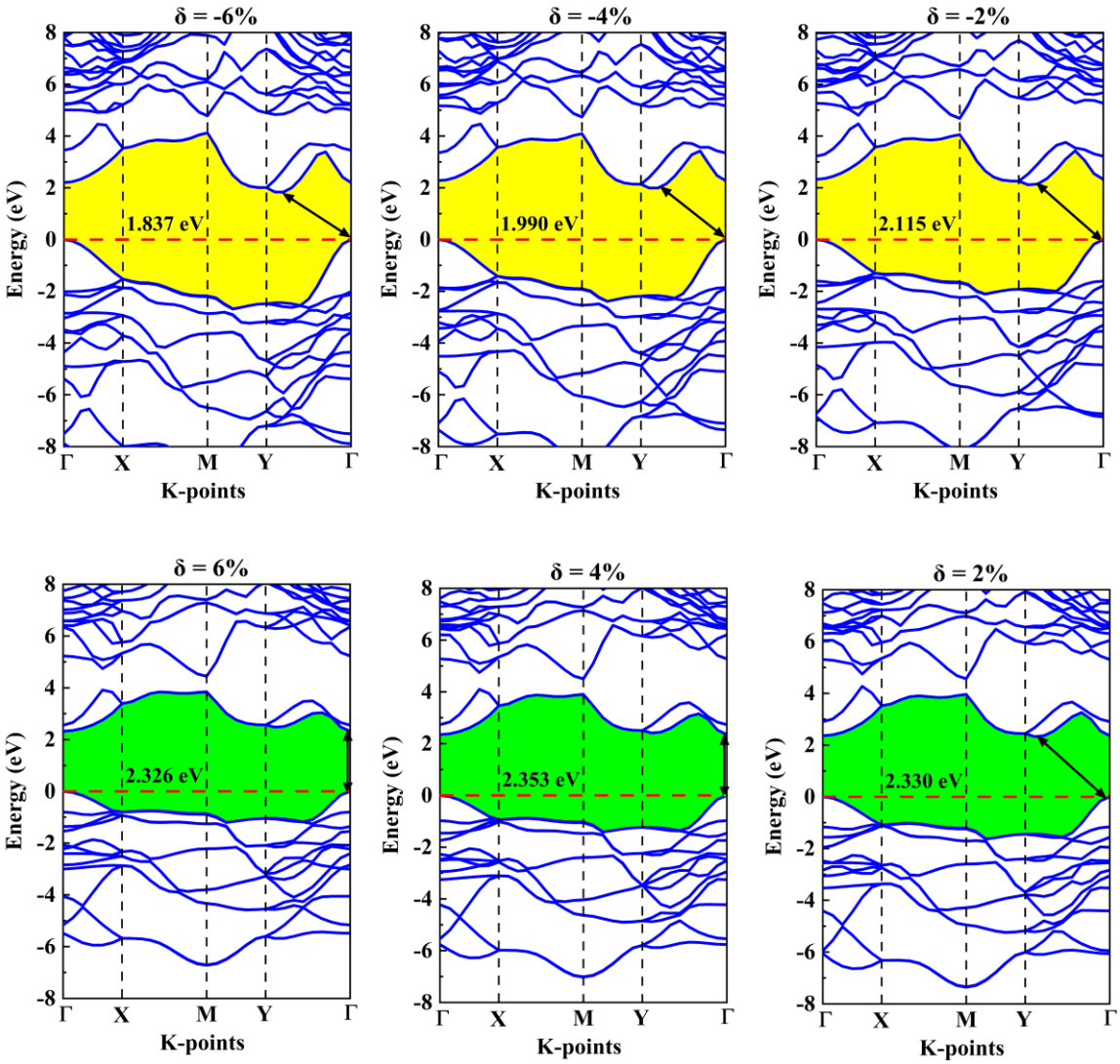

Fig. (3.5). The band structure of AlBrSe monolayer under the strain effect using the HSE06 method.

Remarkably, the bandgap can be modulated by changing the biaxial strain, which is beneficial to achieving optimal electronic performance. On the other hand, the band-edge potentials under the biaxial strain are systematically evaluated. According to Fig.(3.6), the CBM shift upward and the VBM shifts downward with increasing strains. Thus, the energy gaps decrease in the higher compressive strain values. This behavior confirms that low dimensional materials are extremely sensitive to strain, which includes not only the electronic structure but also the optical properties as can see later.

As mentioned above, the ability to reduce/oxidize might be assessed by aligning the CBM and VBM with respect to the water redox potential levels, thus, the redox potentials (magenta dashed line) of water splitting are presented for comparison. However, as shown in Fig.(3.5), the predicted band gaps of the AlBrSe monolayer under the strain effect with the HSE06 functional are in the range of (1.837–2.353) eV, demonstrating that a significant proportion of solar light might be captured by these materials. A semiconductor must have an acceptable bandgap for photocatalytic water splitting as well as good band edge locations for the reduction and oxidation potentials. Furthermore, the strain also affects the positioning of the band edges. The bandgap of AlBrSe monolayer moves from 2.231 to 2.353 eV (at 4%) and 1.837 (at -6%), and the corresponding CBM shifted to -4.070 (4%) and -4.328 (-6%), whereas VBM shifted to -6.423 (4%) and -6.165 (-6%). Therefore, photocatalytic activity can be characterized by the position of strain (biaxial or uniaxial). However, our outcomes show that the photocatalytic activity of the AlBrSe monolayer is an excellent material for water splitting with the strain from -6% to 6%.

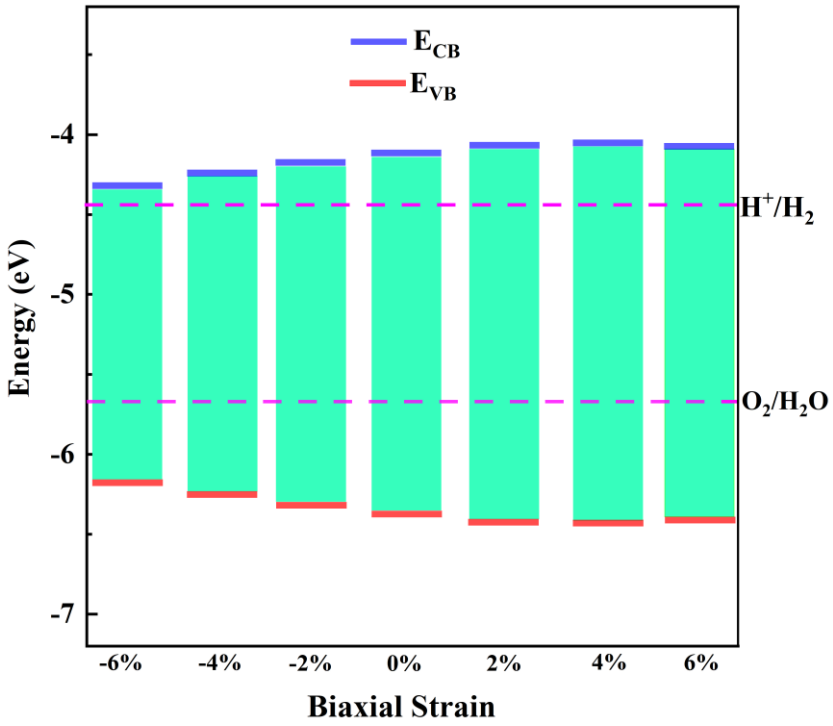

Fig. (3.6). The band-edge potential under biaxial strain.

Because the DOS is closely related to the modification of the energy gaps due to strain, one can observe the change and extension of the peaks belonging to the orbitals participating in the VBM and CBM as shown in Fig.(3.7). We can also see that there is a decrease in the height of the peaks in the density of state in the case of compression strain compared to a very small increase in the height at tensile strain.

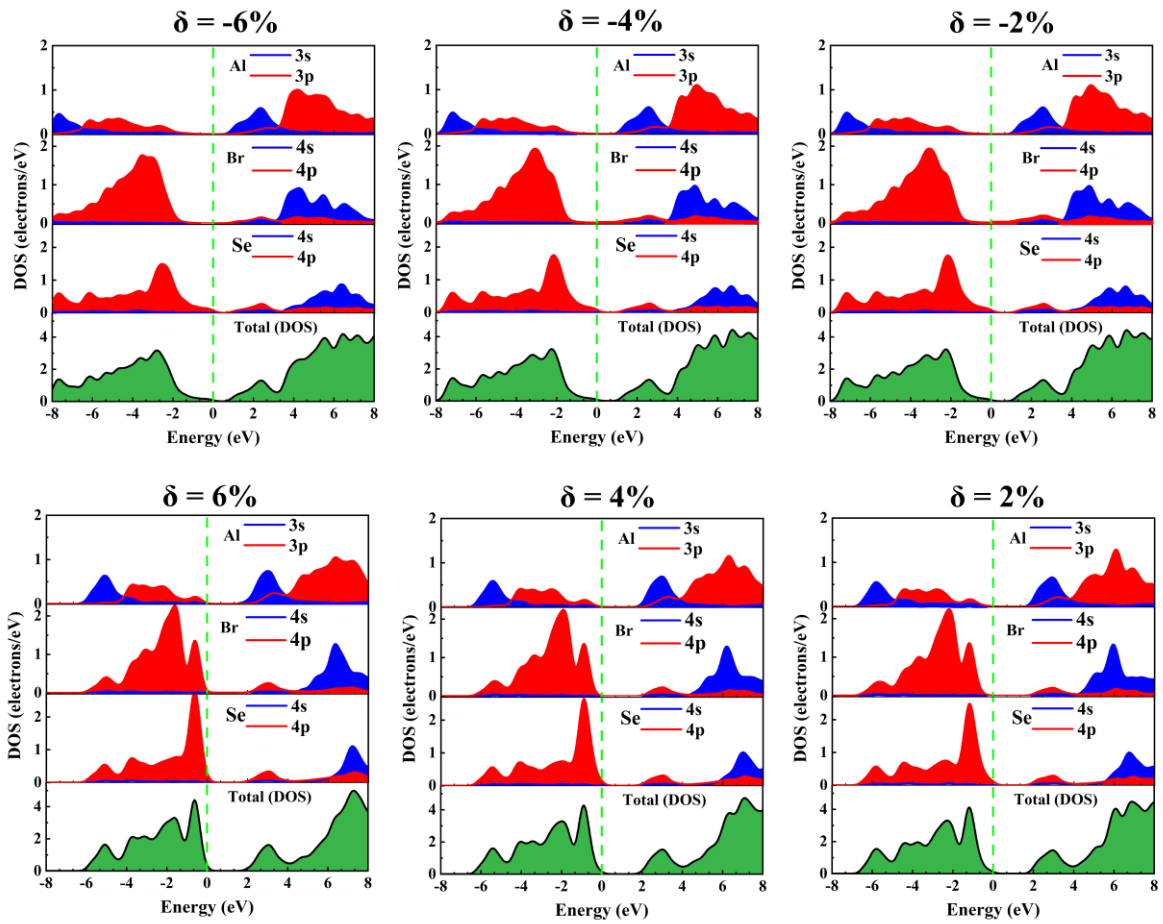

Fig. (3.7). The total and partial density of the state of the AlBrSe monolayer at different strains.

3.1.4 Optical properties under the strain effect

Understanding the behavior of materials as they interact with light, particularly 2D monolayers, which are extraordinarily sensitive to light, requires a thorough comprehension of optical properties. The calculated optical characteristics were implemented over the photon energy range of 0 to 16 eV. At first, the dielectric function was studied, as it was known that this function is of great importance because it gives most of the necessary optical data for all materials. The equilibrium state's real dielectric constant (unstrained) is 2.47, which takes a greater value from tensile and compressive strain.under the effect of compression strain, the values of ε_1

are 2.26, 2.3, and 2.36 for -2%, -4%, and -6%, respectively, while under the tensile strain, ε_1 has lower values, which are about 2.17, 2.14, and 2.12 at 2%, 4%, and 6%, respectively.

Afterwards, the dielectric function grows progressively as the photon's energy increases until it achieves its maximum values, which are 4.13 and 2.68 at -6% and 6%, respectively, these values are exactly located at the photon energy of 6.16 eV and 4.48 eV, respectively, as depicted in Fig. (3.8) (a). The dielectric function indicates the polarization and energy storage that can be utilized in piezoelectric devices. When the photon's energy exceeds 6 eV, ε_1 begins to rapidly decrease, attaining a negative value in the range of 8 eV to 10.4 eV, except at 6%, which has no negative value. On the other hand, the imaginary component (ε_2) of the dielectric function represented the loss due to the absorption and reflection as well as electron vibration at the plasma frequency. It is found that the highest peak of ε_2 is approximately 5 at -6%, while its lowest peak is 2.72 at 6%, as shown in Fig.(3.8) (b). Overall, the compressive strain leads to the improvement of the peak of the dielectric function better than the tensile strain. The second important optical function is the absorption coefficient which measures the effective absorption area of this layer. It was found that the absorption coefficient peak at the pristine state (without strain) is about 13.8×10^4 cm^{-1} at the photon energy of 8.02 eV, while in the visible light region reaches 6.13×10^3 cm^{-1} located precisely at an energy of 3.13 eV. Under the strain effect, the absorption coefficient can be reached 18.9×10^4 cm^{-1} at 7.98 eV at -6%, as shown in Fig. (3.8) (c).

The optical conductivity is primarily determined by the electrons that absorb the energy of the incident photon which are larger or equal to the energy gap, allowing it to transition from VB to CB. It was found that the conductivity of the AlBrSe monolayer has one characteristic peak identical

to the preceding one in the absorption coefficient, with a value of 2.41 at an energy of 7.53 eV for the unstrained state (0%). The peaks of conductivity under the strain effect range from 4.41 (at -6%) to 2.68 (at 6 %), all the peaks are situated in the ultraviolet (UV) region. After that, the peaks vanish abruptly with increasing photon energy, as shown in Fig.(3.8) (d). This decrease is attributed to the failure of the utilization of the increased photon energy to excite and transfer electrons to the CB. The refractive index was calculated to know the extent of its use in optical applications represented in mirrors and lenses, the higher the refractive index, the higher the clarity of the image. The refractive index is closely related to the dielectric constant, as its first appearance at 0 energy was about 1.5 in the unstrained state (0%), and the highest and lowest value under the influence of strain were 1.54 and 1.45 for 6% and -6%, respectively. When the energy of the photon increases, the value of the refractive index increases until it reaches its highest value at -6% and its lowest value at 6%, which are 2.15 and 1.7, respectively, all of which are in the UV region. After that, its value decreases when the incident photon energy increases, as shown in Fig.(3.8)(e). One can find that the maximum reflectivity peak in the original condition (without strain) is approximately equal to 22 %. Under the influence of the strain, the highest reflectivity peaks range from 19 % to 34 % at strains 6% and -6%, respectively. These peaks are in the UV region. In general, the compressive strain leads to an increase in the reflectivity peaks, in contrast to the tensile strain, which led to a decrease in the reflectivity peaks, as shown Fig.(3.8) (f). This feature can be exploited in solar cell bottom layer paint to reflect penetrating photons that can form excitons or be used in photocatalysis. From here, the compressive strain has improved the optical properties.

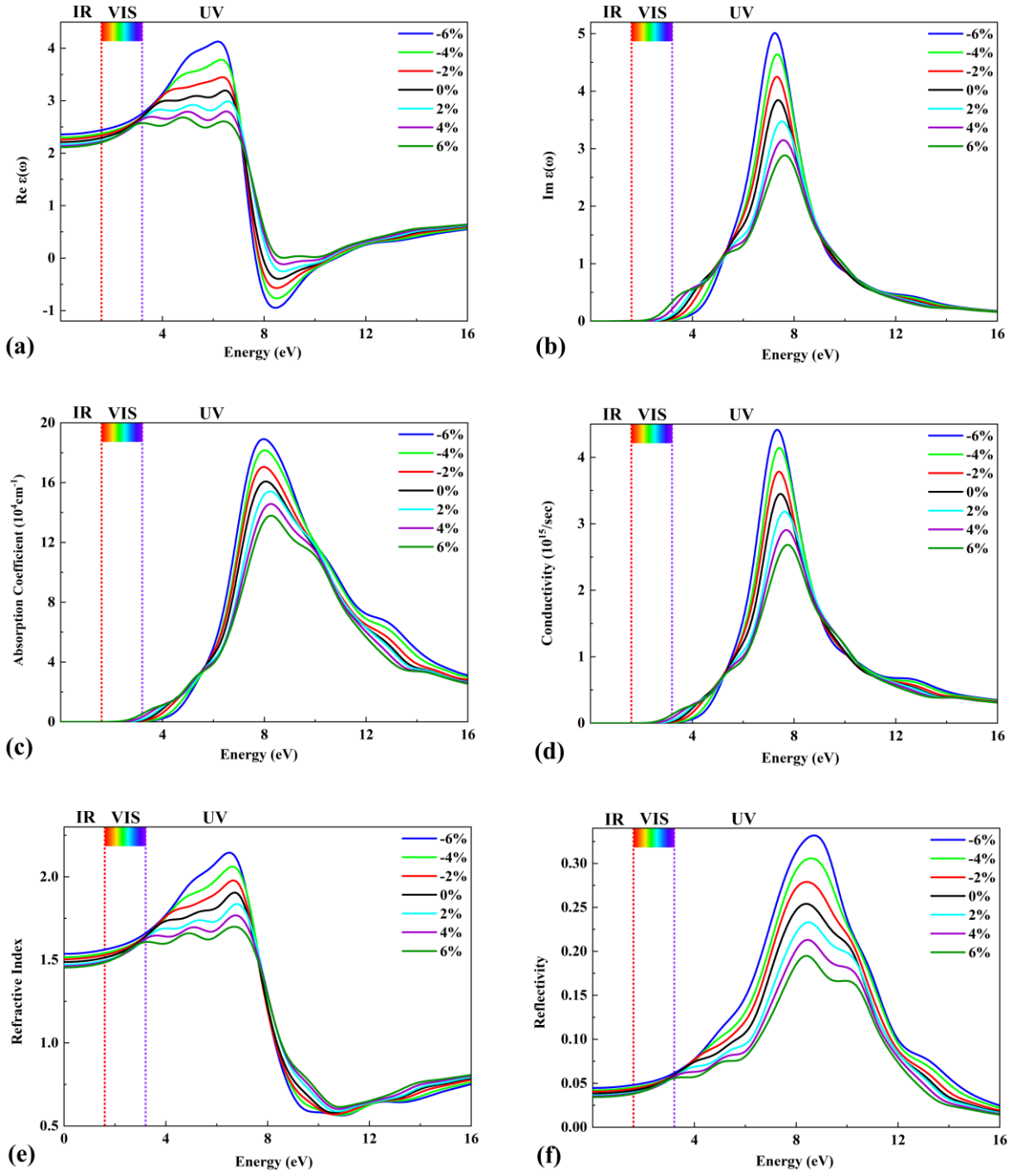

Fig.(3.8): The optical properties as a function of the photon energy of AlBrSe monolayer.

3.2 AlBrS two-dimensional monolayer

3.2.1 Structural and electronic properties

The compound AlBrS is a two-dimensional monolayer compound and this is the chemical formula for this class. The lattice parameters of the AlBrS are *a*= 3.509 Å, *b*=4.824 Å while for c =22 Å they are kept constant to prevent interaction between neighboring layers. The atoms in the monolayer are linked by strong covalent bonds. The atoms of the three elements are distributed in the same way that was mentioned in the previous single layer as shown in Fig. (3.9). The parameters of the geometric structure of the monolayer at equilibrium are summarized as follows the bond length of Al-Br (2.520 Å), while the bond length of Al-S1, Al-S2 are (2.401 Å) and (2.438 Å), respectively. As a result of this difference in the length of the bonding bonds between the atoms of the mentioned elements, four angles appeared as shown in Fig. (3.9), then θ_1 (88.282°), θ_2 (93.905°), θ_3 (88.907°), and θ_4 (84.334°). The thickness of AlBrS less than AlBrSe monolayer is 5.698 Å.

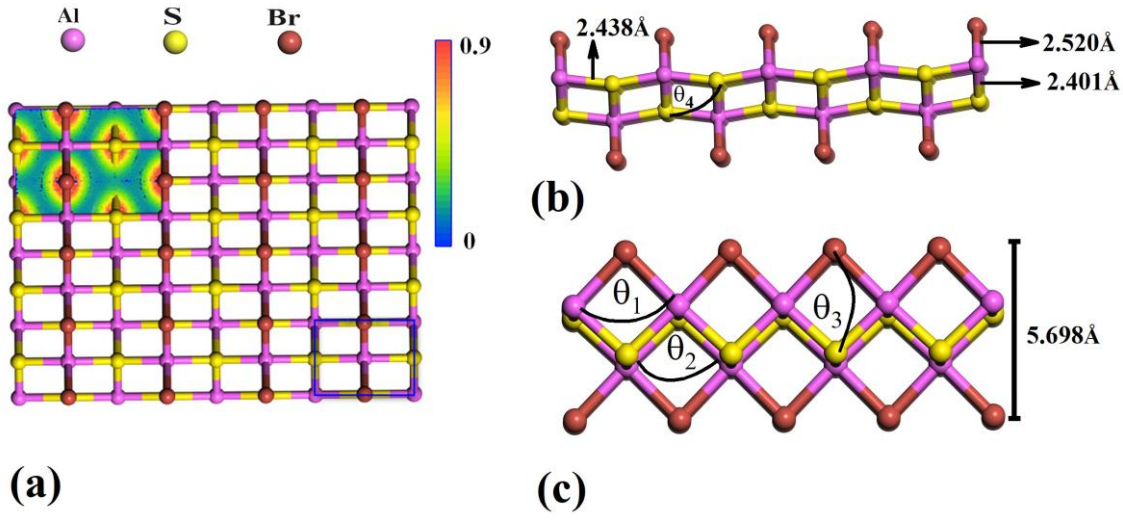

Fig. (3.9): (a) Top and (b,c) side views of the optimized structure of the AlBrS monolayer. The snapshot in (a) refers to the electron localization function.

The electron localization function AlBrSe is exhibited In Fig. (3.9)(a), with delocalized (0.5) and fully localized (0.9) electrons denoted by green and red areas, respectively, and very low electron density denoted by the blue region (0.0). The red area shows a high concentration of electronic density focused around the S and Br atoms, whereas the blue area represents a low electronic density. Perhaps the reason behind this is the atomic numbers of S and Br are greater than Al. The phonon band, which does not contain any negative frequency for the acoustic and optical branches, was used to validate the dynamic stability, as seen in Fig(3.10)(a).

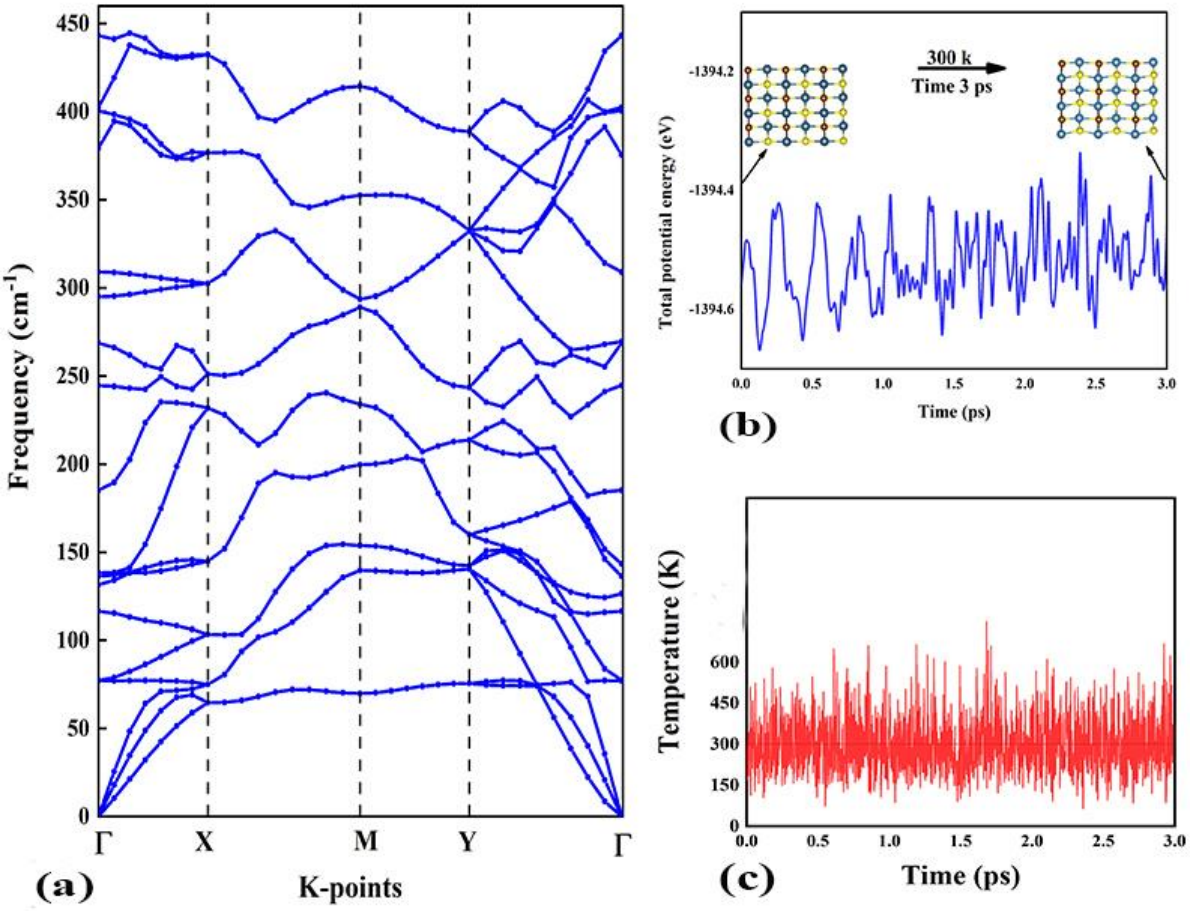

Fig. (3.10). (a) The phonon dispersion curve, (b) total potential energy as a function of time variation, and (c) temperature as a function of AIMD steps at 300 K of AlBrS monolayer.

The forcite program connected with AIMD was used to detect negligible fluctuations in the total energies of this monolayer, without bond breakage but there is a ripple in the bonds due to the thermal effect, confirming their strong thermodynamic stabilities at a temperature of 300 K, as shown in Fig. (3.10)(b) and (c). The expected electronic band structure for the AlBrS was calculated by PBE and HSE06 functional as illustrated in Fig (3.11)(a). The AlBrS has a direct bandgap of about 2.221 eV (PBE)/3.039 eV(HSE06), in which the valence band maximum (VBM) and the conduction band minimum (CBM) lie at the Γ point.

Fig. (3.11)(b) is depicted the partial state density (PDOS) for each element that participation in layer formation. The results obtained are quite similar to those found in the AlBrSe layer because it has the same geometric structure. The valence band near the Fermi level is mainly determined by the contribution of all the p orbitals of the Al, Br and S atoms. Emphasizing that the contribution of Br and Se atoms is much greater than that of Al due to the large atomic numbers of Br and Se elements relative to the atomic number of Al, this is in complete agreement with the electron localization density. While the participation of orbital 3s, which belongs to the element Al, was revealed in the energy range beyond 3eV. In the CBM, one can observe a complete different approach than in the VBM. There is a very clear electronic void in the region adjacent to the Fermi level up to 2 eV and this is consistent with the energy gap. Participation starts from 2 eV for orbital 3s for Al and active participation for 4s for Br. There is also the contribution of the p orbital to the three elements, the most important of which is the orbital that belongs to the Al atom.

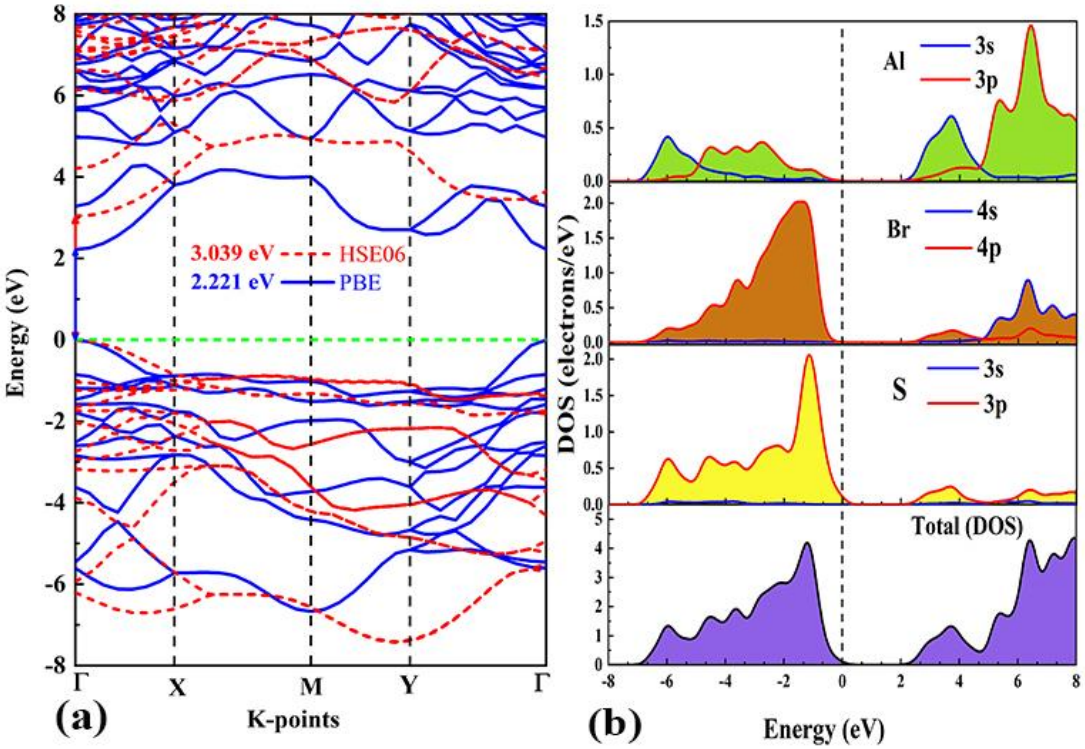

Fig. (3.11): (a) The calculated band structure by PBE and HSE06 methods and (b) partial and total density of state of AlBrS monolayer.

From Fig. (3.12)(a) the AlBrS layer is considered in the proposed project as an active photocatalyst in the UV and VIS light region because it fulfills the conditions that must be available in the photocatalysts for water splitting. The E_{VB} is equal to -3.82eV (higher than redox potential) and the E_{CB} is equal to -6.86eV (lower than the oxidation potential). The calculated work function of the monolayer is equal to 6.015 eV as seen in Fig. (3.12)(b).

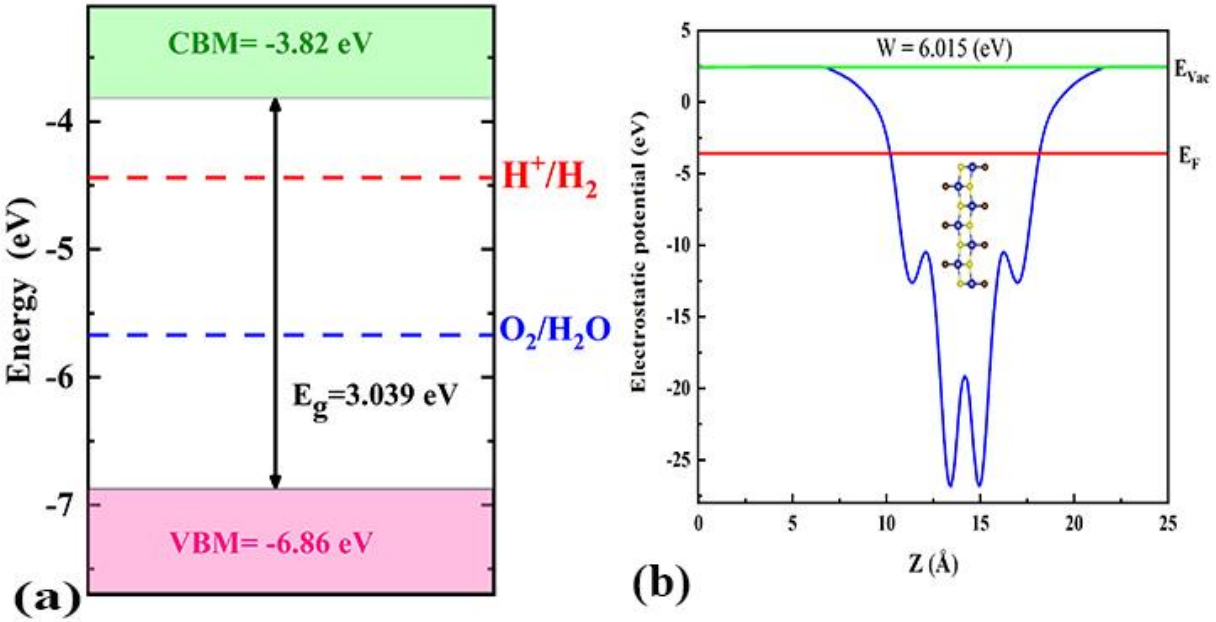

Fig. (3.12): (a) The AlBrS band alignment demonstrates the ability of the layer to s water splitting and (b) the work function of the AlBrS monolayer.

3.2.2 Strain effect on AlBrS monolayer

The electronic and optical properties can be modified by introducing a biaxial strain. The energy gaps, DOS, band-edge potential, and optical properties were investigated under the influence of tensile and compressive strains on the monolayer. The monolayer was subjected to tensile and compressive stress within a range of 6% to -6%. The electronic structure is very sensitive to the biaxial strain, as a change in the energy gap was observed under the influence of strain, in all cases, the energy gaps are less than they are in the case of equilibrium. The VBM and CBM maintain their position at Γ point. The energy gaps under the action of tensile stress are as follows 3.023 eV ,2.987 eV, and 2.933 eV at 2%,4%, and 6%, while under compression strain they take the following order 3.034 eV,3.005 eV and 2.949 eV at -2%, -4%, and -6% respectively . The energy gaps at 6% and -6% are very close to each other as shown in Fig (3.13). This means that

perhaps after this range of stress the band structure takes a constant value. Since the density of states is closely related to the modulation of the energy gaps due to stress, one can observe the shift and extension of the peaks belonging to the orbitals involved in VB and CB as shown in Fig. (3.14). From Fig. (3.15), the band alignment behavior under biaxial stress is almost imperceptible due to the slight gradient occurring in the energy gap. All the energy gaps mentioned under or without strain confirm that the layer is semiconducting and can be used in the VIS and UV range.

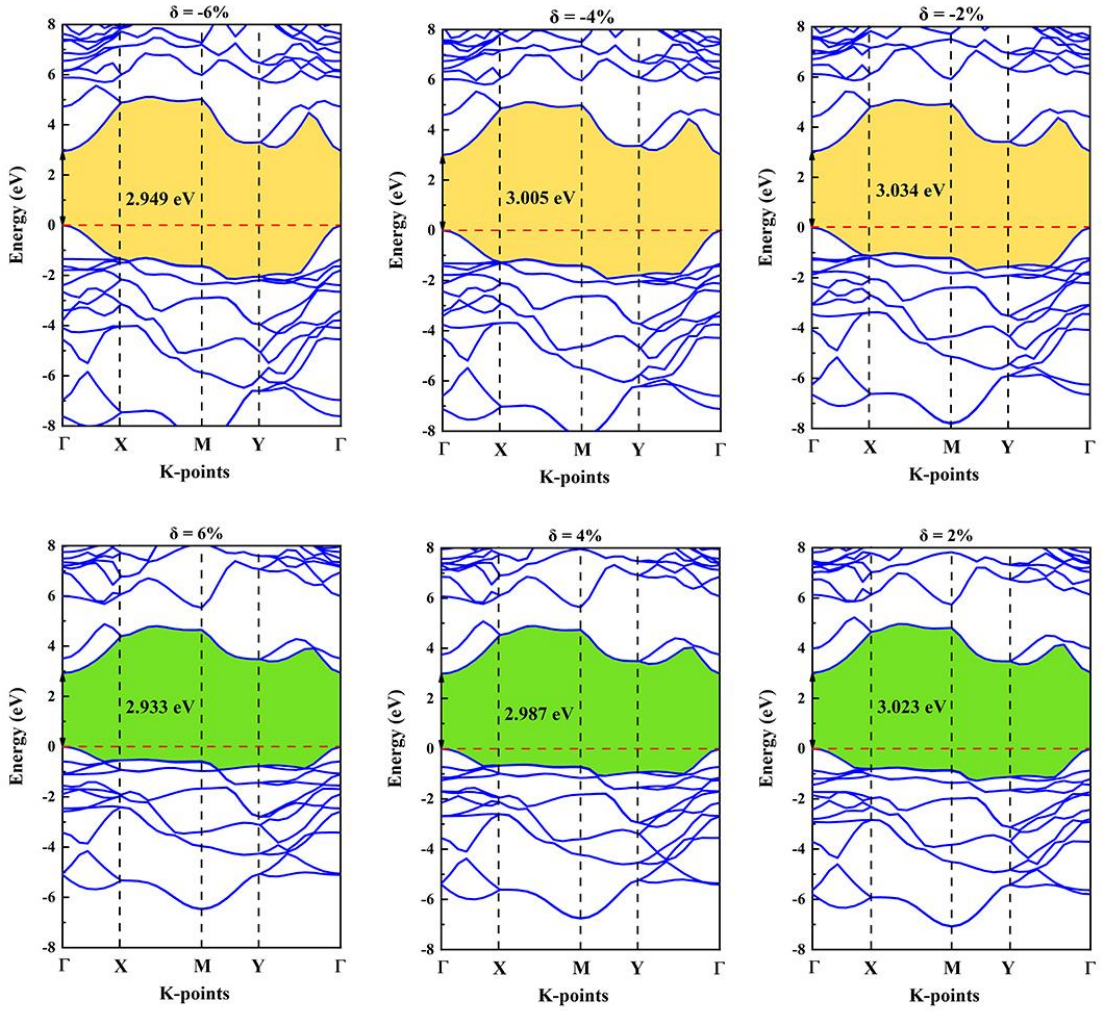

Fig. (3.13): The bandgap under the biaxial strain of AlBrS monolayer.

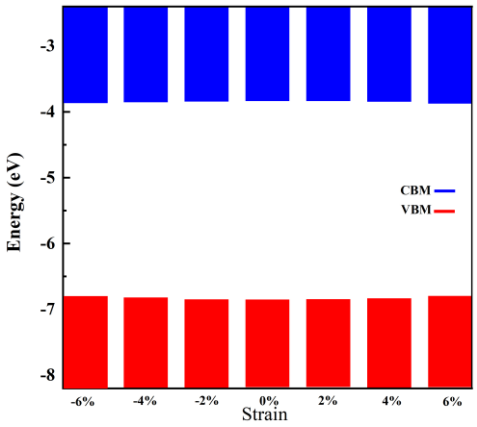

Fig. (3.14): The band alignment under the biaxial strain of AlBrS monolayer.

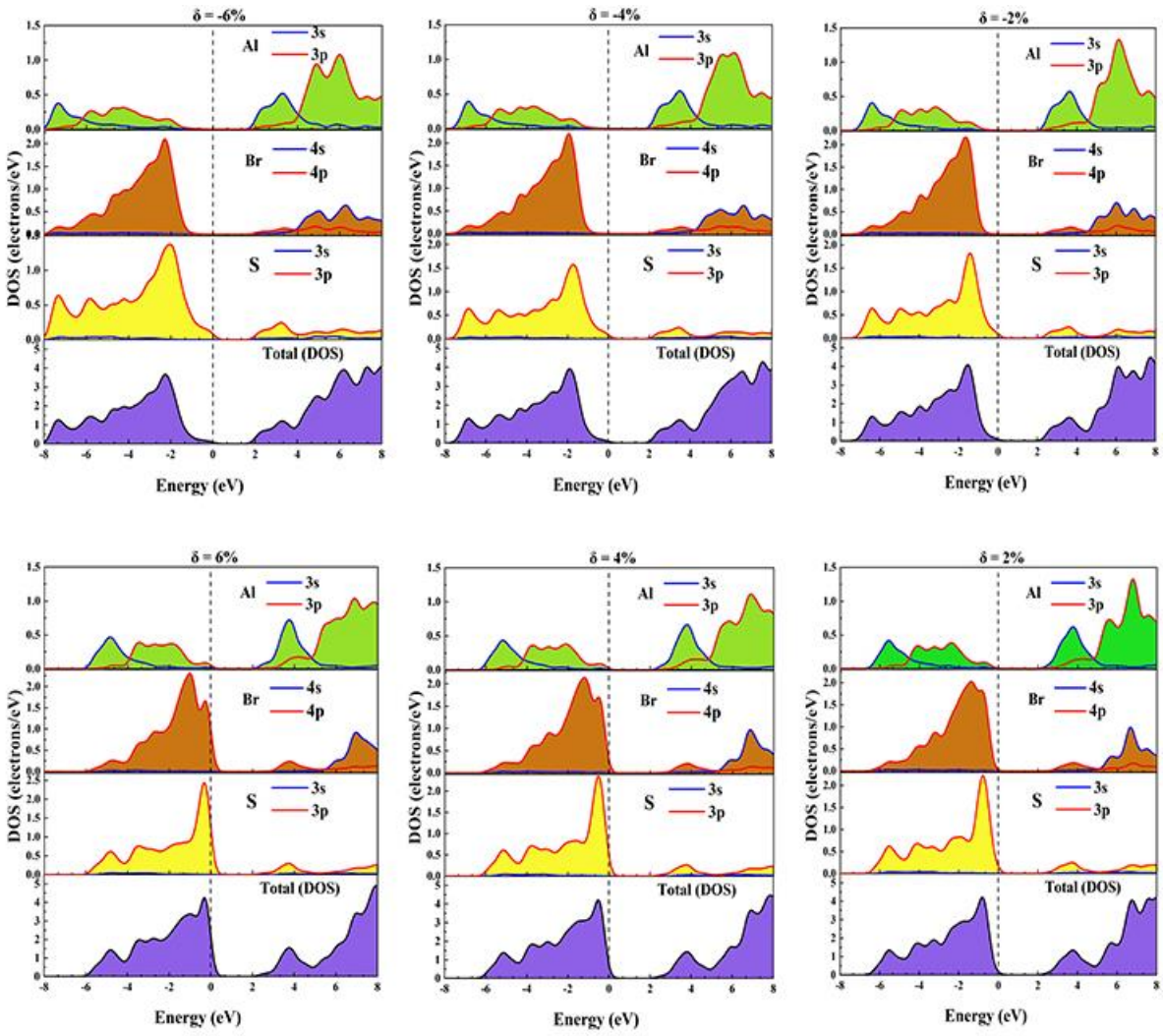

Fig. (3.15): The project total and partial density of the state of the AlBrS monolayer.

3.2.3 Optical properties under strain

It is necessary to study the optical properties of single-layer 2D nanomaterials to understand the sensitivity of these materials to the direction of light. These materials form the basis of modern science in the applications of photovoltaic devices. These properties are implemented in the range (0-16 eV). The first optical function focused on is the dielectric function as a function of photon energy, which refers to polarization and energy storage, and consists of two parts. The real part (ε_1) and the imaginary part (ε_2). The dielectric constant in the equilibrium state (ε_1) is (2.13), Then it begins to grow gradually in the form of peaks, where it reaches the highest value at (3.32). After that, it starts declining towards the negative area, where it is within the range of values (8.33-10.8 eV). The (ε_1) values of the compression strain are 2.18, 2.23, and 2.29 for -2%, -4%, and -6 %, respectively, while for the tensile are 2.1, 2.07, and 2.11 for 2%, 4% and 6%, respectively. The values of (ε_1) at compressive strain are higher than the values at the tension. The dielectric function begins to grow gradually with the increase in the energy of the incident photon. The highest values of ε_1 values are (4.36) and (2.67) at -6 %, 6% which are located at the energy (6.84ev) and (6.38ev) respectively as seen in Fig.(3.16)(a). The ε_2 is illustrated in Fig. (3.16) (b), which represents the loss resulting from absorption, reflection, and electron vibration. Its value in equilibrium ε_2 is (3.88) at (7.76 eV). The highest value was determined in the case of compression (-6%), which is about(5.12) at (7.44ev), and the lowest value at the tension(6%), which is estimated at 2.84 at 8 eV. The absorption coefficient, the second most essential optical function Through which the absorption area is known in this layer, is shown in Fig. (3.16) (c). The absorption coefficient increases with compression and decreases

with tension, whereas the unstrained state takes a value located between the tensile and compressive state, which is about is ($17\times10^{4}cm^{-1}$) at (8.34 eV), It is worth mentioning that absorption in the visible light region reaches($1.6\times10^{3}cm^{-1}$) at (3.15 eV). The absorption process begins from the VIS region to the UV region where the maximum peaks are concentrated in the ultraviolet region. The absorption coefficient takes values ($19.9\times10^{4}cm^{-1}$,$14.5\times10^{4}cm^{-1}$) for (-6% and 6%) respectively as shown Fig. (3.16)(c) . Optical conductivity is primarily determined by the electrons that absorb the energy of the incident photon and are larger or equal to the energy gap, allowing it to transition from VB to CB. Fig. (3.16)(d) exhibits that the conductivity has one characteristic peak identical to the preceding one in the absorption coefficient, with a value of $3.65\times10^{-15}\ \frac{1}{s}$ at an energy of 7.83eV for the equilibrium state (0%). Under strain, the conductivity ranges from $4.71\times10^{-15}\ \frac{1}{s}$ to $2.8\times10^{-15}\ \frac{1}{s}$ for -6% and 6 % all situated in the UV region, after which the peaks vanish abruptly with increasing photon energy. This decrease is attributed to the failure to take advantage of the increase in photon energy to excite the electrons and transfer them to the CB. The refractive index of the monolayer was calculated to know the extent of its use in optical applications represented in mirrors and lenses, the higher the refractive index, the higher the clarity of the image. The refractive index is closely related to the dielectric constant, as its first appearance at zero energy was about 1.46 for the equilibrium state, and the highest and lowest value under the influence of strain were 1.51 and 1.45 for -6% and 6%, respectively. When the energy of the photon increases, the value of the refractive index increases until it reaches its highest value at -6 and its lowest value at 6, which is 2.19 and 1.7, respectively, all of which are in the ultraviolet

region. After that, its value decreases when the energy of the photon incident increases as shown in Fig. (3.16)(e).

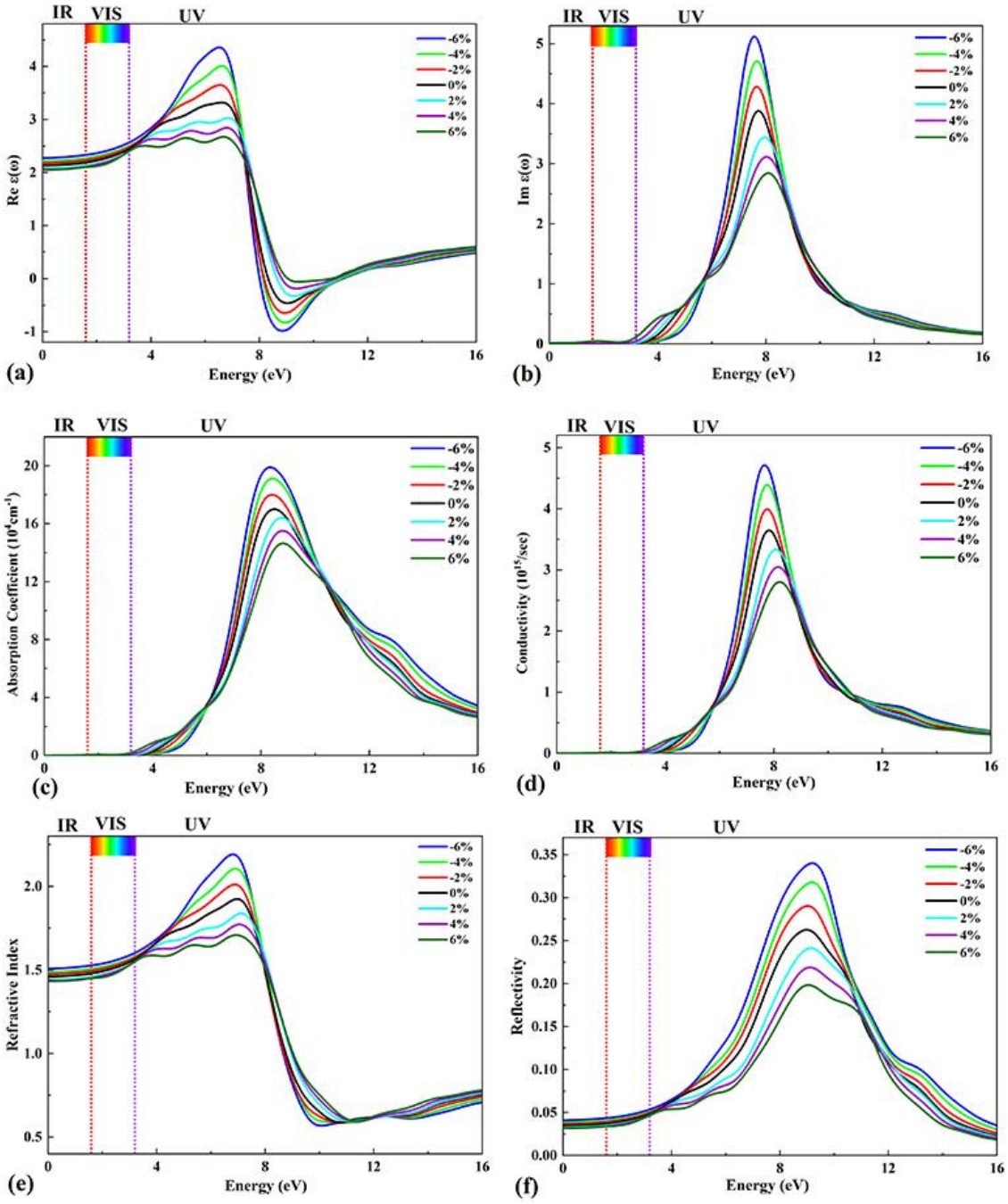

Fig. (3.16): The optical properties as a function of the photon energy of AlBrS monolayer.

The final optical function that has been addressed is reflection. The UV area encompasses all reflectance values. The reflectance range is 19.8% at tensile (6%) to 34% at compression strain (-6%), while the value of reflectivity an equilibrium state (0%) is equivalent of 26.3% as shown Fig.(3.16)(f).This feature can be exploited in solar cell bottom layer paint to reflect penetrating photons that can form excitons or be used in photocatalysis. In general, and depending on the electronic and optical properties, this layer can be used in the manufacture of solar cells and photocatalysts, as well as capacitors in microelectronic devices.

Chapter Four

Conclusions and Suggestions

4.1 Conclusions

1. The two layers have the same geometric composition which is an orthorhombic lattice with space group Pmmn (D2h-13, No. 59), With slight differences in the thickness of the layers, the bond lengths, the angles, and the lattice constants.
2. The kinetic and thermodynamic stabilities of the monolayers of (AlBrSe, AlBrSe) were validated by investigating the phonon carve and ab-initio molecular dynamic molecular dynamics.
3. The monolayers are semiconductors, where the AlBrSe layer has an indirect energy gap (2.231 eV) and the location of the VBM at Γ point and the CBM at Γ -Y point, while the layer of AlBrS has a direct bandgap which is equal (3.039 eV) lied at Γ according to the HSE06 functionals.
4. The effect of biaxial strain can enhance the band structure of 2D monolayers effectively, as we observe the energy gap shift from indirect to direct at 4% and 6% strain for the AlBrSe layer, while the AlBrS layer kept its position with a change in the energy gap values of both layers according to the applied strain.
5. The effect of biaxial strain can enhance the optical efficiency of these 2D monolayers.
6. The dielectric constant in the equilibrium state (ε_1) of AlBrSe monolayer is (2.47), whereas it reaches the highest value at (3.32), while the AlBrS monolayer is 2.13 and the maximum value 3.33.
7. The dielectric constant under biaxial strain has a maximum value at -6% (compressive strain) and a minimum value at 6% (tensile strain) for both monolayers.
8. The absorption coefficient peak at the pristine state (without strain) of AlBrSe is about 13.8×10^4 cm^{-1} at the photon energy of 8.02 eV,

while in the visible light region reaches 6.13×10^{3} cm^{-1} located precisely at an energy of 3.13 eV, whereas of AlBrS is ($17\times10^{4}cm^{-1}$) at (8.34 eV), and in the visible light region reaches ($1.6\times10^{3}cm^{-1}$) at (3.15 eV).

9. The optical conductivity peak at the pristine state of AlBrSe is about $2.41 \times 10^{15}\ S^{-1}$ at an energy of 7.53 eV for the unstrained state (0%), and for AlBrS which equals $3.65 \times 10^{-15}\ S^{-1}$ at an energy of 7.83 eV.
10. The absorption coefficient and optical conductivity of the two monolayers behave similarly under the impact of strain, they grow when compressed and reach their highest values at -6 %, and they drop when tensile and reach their lowest values at 6 %.
11. The values of reflectivity and refraction are also concentrated in the ultraviolet region for both monolayers
12. These monolayers can absorb light in a wide range of visible-ultraviolet regions. Thus, the optimal application is as photocatalysts for water splitting based on the results obtained in addition to its utility in the photovoltaic and optoelectronic devices in these areas.

4.2 Suggestions for Future Works:

The following studies can be suggested for future work:

1. Study of the effect of electric field on the photoelectric properties of two-dimensional monolayer materials using the DFT calculations.
2. Investigation of the vibrational, mechanical, thermal, and magnetic properties of AlBrSe and AlBrS monolayers.
3. Studying the impact of vacancies and points defects on the electronic and optical properties AlBrSe and AlBrS monolayers.

4. Study of the effect of spin coupling on the structural, electronic, and optical properties of AlBrSe and AlBrS.
5. Revealing the doping effect on the electronic and optical properties of AlBrSe and AlBrS monolayers.
6. Creating a heterostructures layer from the two mentioned layers with different staking and, then checking its optical and electronic properties using DFT calculations.

References

Reference

[1] P.W. Cyr, M. Tzolov, M.A. Hines, I. Manners, E.H. Sargent, G.D. Scholes, Quantum dots in a metallopolymer host: studies of composites of polyferrocenes and CdSe nanocrystals, J. Mater. Chem. 13 (2003) 2213–2219.

[2] K.D. Sattler, Handbook of nanophysics: principles and methods, CRC press, 2010.

[3] C.N. Anumol, M. Chithra, S. Rout, S.C. Sahoo, Effect of Magnesium Substitution on Structural and Magnetic Properties of Nickel Ferrite Nanoparticles, J. Supercond. Nov. Magn. 33 (2020) 1611–1617. https://doi.org/10.1007/s10948-019-05192-8.

[4] M.S. Dresselhaus, G. Dresselhaus, Intercalation compounds of graphite, Adv. Phys. 30 (1981) 139–326.

[5] Y. Zhang, J.P. Small, W. V. Pontius, P. Kim, Fabrication and electric-field-dependent transport measurements of mesoscopic graphite devices, Appl. Phys. Lett. 86 (2005) 1–3. https://doi.org/10.1063/1.1862334.

[6] J.M. Pereira, F.M. Peeters, R.N. Costa Filho, G.A. Farias, Valley polarization due to trigonal warping on tunneling electrons in graphene, J. Phys. Condens. Matter. 21 (2008) 45301.

[7] G.A. Mansoori, Principles of nanotechnology: molecular-based study of condensed matter in small systems, World Scientific, 2005.

[8] C.D. Pegden, R.E. Shannon, R.P. Sadowski, Introduction to simulation using SIMAN, McGraw-Hill, New York, USA, 1995.

[9] H. Zhang, Ultrathin two-dimensional nanomaterials, ACS Nano. 9 (2015) 9451–9469.

[10] Q. Li, S.-M. Koo, C.A. Richter, M.D. Edelstein, J.E. Bonevich, J.J. Kopanski, J.S. Suehle, E.M. Vogel, Precise alignment of single nanowires and fabrication of nanoelectromechanical switch and other test structures, IEEE Trans. Nanotechnol. 6 (2007) 256–262.

[11] R.A. Ghazi, D. Ali Sabur, R.S. Al-Hasnawy, H.O. Muhsen, B.B. Kadhim, F.M. Salim, H.R. Jappor, A.M. Ali, Structural, electronic and optical properties of transition metal dichalcogenides layer pts2 (Se2) for Nano devices applications, Key Eng. Mater. 886 (2021) 48–56. https://doi.org/10.4028/www.scientific.net/KEM.886.48.

[12] M.D. Stoller, S. Park, Y. Zhu, J. An, R.S. Ruoff, Graphene-based ultracapacitors, Nano Lett. 8 (2008) 3498–3502.

[13] Y.H. Huang, C.C. Peng, R.S. Chen, Y.S. Huang, C.H. Ho, Transport properties in semiconducting NbS2nanoflakes, Appl. Phys. Lett. 105 (2014) 93106. https://doi.org/10.1063/1.4894857.

[14] K. Ren, R. Zheng, J. Lou, J. Yu, Q. Sun, J. Li, Ab Initio Calculations for the Electronic, Interfacial and Optical Properties of Two-Dimensional AlN/Zr2CO2 Heterostructure, Front. Chem. 9 (2021) 1–7. https://doi.org/10.3389/fchem.2021.796695.

Reference

[15] K.S. Novoselov, A.K. Geim, S. V. Morozov, D.A. Jiang, Y.Y. Zhang, S. V. Dubonos, A.A. Firsov, I. V. Grigorieva, A.A. Firsov, Electric Field Effect in Atomically Thin Carbon Films, Science (80-.). 306 (2004) 666–669. https://doi.org/10.1126/science.1102896.

[16] L. Malikova, F.H. Pollak, O. Gorea, A. Korotcov, Modulation spectroscopy study of a strained layer GaAs/GaAsP multiple quantum well structure, J. Electron. Mater. 29 (2000) 1346–1350. https://doi.org/10.1007/s11664-000-0136-y.

[17] G. Abstreiter, H. Brugger, T. Wolf, H. Jorke, H.J. Herzog, Strain-induced two-dimensional electron gas in selectively doped Si/SixGe1-x superlattices, Phys. Rev. Lett. 54 (1985) 2441–2444. https://doi.org/10.1103/PhysRevLett.54.2441.

[18] Y. Ishikawa, K. Wada, J. Liu, D.D. Cannon, H.C. Luan, J. Michel, L.C. Kimerling, Strain-induced enhancement of near-infrared absorption in Ge epitaxial layers grown on Si substrate, J. Appl. Phys. 98 (2005) 013501. https://doi.org/10.1063/1.1943507.

[19] J. Annett, G.L.W. Cross, Self-assembly of graphene ribbons by spontaneous self-tearing and peeling from a substrate, Nature. 535 (2016) 271.

[20] N. Mohta, S.E. Thompson, Mobility enhancement, IEEE Circuits Devices Mag. 21 (2005) 18–23.

[21] A. Fujishima, K. Honda, Electrochemical Photolysis of Water at a Semiconductor Electrode, Nature. 238 (1972) 37–38. https://doi.org/10.1038/238037a0.

[22] A. Fujishima, T.N. Rao, D.A. Tryk, Titanium dioxide photocatalysis, J. Photochem. Photobiol. C Photochem. Rev. 1 (2000) 1–21.

[23] L. Casey, Y.J. Do, G. Goutzioulis, A. Kumar, S. Kuo, J. Lawrence, T. McGahern, M. McKenzie, J. Roller, R. Rose, Energy and climate change: nonpartisan policies for the next US President, (2019).

[24] A. Miketa, D. Saygin, R.G. Ferroukhi, D. Hawila, A. Kojakovic, N. Nagpal, Africa 2030: Roadmap for a renewable energy future, Abu Dhabi. (2015).

[25] K. Takanabe, Solar water splitting using semiconductor photocatalyst powders, Sol. Energy Fuels. 371 (2015) VII, 327.

[26] M.S. Dresselhaus, I.L. Thomas, Alternative energy technologies, Nature. 414 (2001) 332–337.

[27] X. Lv, W. Wei, Q. Sun, F. Li, B. Huang, Y. Dai, Two-dimensional germanium monochalcogenides for photocatalytic water splitting with high carrier mobility, Appl. Catal. B Environ. 217 (2017) 275–284. https://doi.org/10.1016/j.apcatb.2017.05.087.

[28] M.M. Obeid, C. Stampfl, A. Bafekry, Z. Guan, H.R. Jappor, C.V. Nguyen, M. Naseri, D.M. Hoat, N.N. Hieu, A.E. Krauklis, T.V. Vu, D. Gogova, First-principles investigation of nonmetal doped single-

Reference

layer BiOBr as a potential photocatalyst with a low recombination rate, Phys. Chem. Chem. Phys. 22 (2020). https://doi.org/10.1039/d0cp02007a.

[29] A.O. Muhsen Almayyali, H.O. Muhsen, M. Merdan, M.M. Obeid, H.R. Jappor, Two-dimensional ZnI2 monolayer as a photocatalyst for water splitting and improvement its electronic and optical properties by strains, Phys. E Low-Dimensional Syst. Nanostructures. 126 (2021) 114487. https://doi.org/10.1016/j.physe.2020.114487.

[30] Z. Haman, N. Khossossi, M. Kibbou, I. Bouziani, D. Singh, I. Essaoudi, A. Ainane, R. Ahuja, Computational identification of efficient 2D Aluminium chalcogenides monolayers for optoelectronics and photocatalysts applications, Appl. Surf. Sci. 556 (2021) 149561. https://doi.org/10.1016/J.APSUSC.2021.149561.

[31] Z. Haman, N. Khossossi, M. Kibbou, I. Bouziani, D. Singh, I. Essaoudi, A. Ainane, R. Ahuja, Janus Aluminum Oxysulfide Al2OS: A promising 2D direct semiconductor photocatalyst with strong visible light harvesting, Appl. Surf. Sci. 589 (2022) 152997. https://doi.org/10.1016/J.APSUSC.2022.152997.

[32] M. Faraji, A. Bafekry, M.M. Fadlallah, H.R. Jappor, C. V. Nguyen, M. Ghergherehchi, Two-dimensional XY monolayers (X = Al, Ga, In; Y = N, P, As) with a double layer hexagonal structure: A first-principles perspective, Appl. Surf. Sci. (2022) 152998. https://doi.org/10.1016/J.APSUSC.2022.152998.

[33] D. Chodvadiya, U. Jha, P. piewak, K.J. Kurzydłowski, P.K. Jha, Potential Anodic Application of 2D h-AlC for Li and Na-ions Batteries, Appl. Surf. Sci. (2022) 153424. https://doi.org/10.1016/J.APSUSC.2022.153424.

[34] M. Demirtas, M.J. Varjovi, M.M. Cicek, E. Durgun, Tuning structural and electronic properties of two-dimensional aluminum monochalcogenides: Prediction of Janus Al2XX′(X/X′:O,S,Se,Te) monolayer, Phys. Rev. Mater. 4 (2020) 114003. https://doi.org/10.1103/PhysRevMaterials.4.114003.

[35] G.S. Khosa, S.K. Tripathi, A.A. Alshaikhi, S. Gupta, R. Kumar, Janus Al2STe monolayer: A prospective thermoelectric material, Solid State Commun. 341 (2022) 114579. https://doi.org/10.1016/J.SSC.2021.114579.

[36] G.S. Khosa, S. Gupta, R. Kumar, First-principles investigations of electronic and thermoelectric properties of Janus Al2SSe monolayer, Phys. B Condens. Matter. 615 (2021) 413057. https://doi.org/10.1016/J.PHYSB.2021.413057.

[37] S. Choopani, M.M. Alyörük, Piezoelectricity in two-dimensional aluminum, boron and Janus aluminum-boron monochalcogenide monolayers, J. Phys. D. Appl. Phys. 55 (2022) 155301.

Reference

https://doi.org/10.1088/1361-6463/AC4769.

[38] L.B. Zhan, C.L. Yang, M.S. Wang, X.G. Ma, Two-dimensional AlBiX3(X = S, Se, Te) monolayers for photocatalytic water splitting hydrogen evolution reaction under the irradiation of solar light, FlatChem. 31 (2022) 100331. https://doi.org/10.1016/J.FLATC.2021.100331.

[39] X. Chen, Y. Huang, J. Liu, H. Yuan, H. Chen, Thermoelectric Performance of Two-Dimensional AlX (X = S, Se, Te): A First-Principles-Based Transport Study, ACS Omega. 4 (2019) 17773–17781. https://doi.org/10.1021/acsomega.9b02235.

[40] T.T. Song, M. Yang, J.W. Chai, M. Callsen, J. Zhou, T. Yang, Z. Zhang, J.S. Pan, D.Z. Chi, Y.P. Feng, S.J. Wang, The stability of aluminium oxide monolayer and its interface with two-dimensional materials, Sci. Reports 2016 61. 6 (2016) 1–9. https://doi.org/10.1038/srep29221.

[41] S. Lin, Y. Wang, Z. Chen, Two-dimensional aluminum monoxide nanosheets: A computational study, Front. Phys. 2018 133. 13 (2018) 1–8. https://doi.org/10.1007/S11467-018-0782-2.

[42] Y. Ma, Y. Dai, W. Wei, X. Li, B. Huang, Emergence of electric polarity in BiTeX (X = Br and I) monolayers and the giant Rashba spin splitting, Phys. Chem. Chem. Phys. 16 (2014) 17603–17609. https://doi.org/10.1039/c4cp01975j.

[43] S. Wen, H. Pan, Y. Zheng, Electronic properties of tin dichalcogenide monolayers and effects of hydrogenation and tension, J. Mater. Chem. C. 3 (2015) 3714–3721.

[44] J.M. Gonzalez, I.I. Oleynik, Layer-dependent properties of SnS 2 and SnSe 2 two-dimensional materials, Phys. Rev. B. 94 (2016) 125443.

[45] M. Safari, Z. Izadi, J. Jalilian, I. Ahmad, S. Jalali-Asadabadi, Metal mono-chalcogenides ZnX and CdX (X = S, Se and Te) monolayers: Chemical bond and optical interband transitions by first principles calculations, Phys. Lett. A. 381 (2017) 663–670. https://doi.org/10.1016/j.physleta.2016.11.040.

[46] B. Wang, X. Niu, Y. Ouyang, Q. Zhou, J. Wang, Ultrathin Semiconducting Bi2Te2S and Bi2Te2Se with High Electron Mobilities, J. Phys. Chem. Lett. 9 (2018) 487–490. https://doi.org/10.1021/acs.jpclett.7b03036.

[47] A.N. Inamdar, N.N. Som, A. Pratap, P.K. Jha, Hydrogen evolution and oxygen evolution reactions of pristine and alkali metal doped SnSe2 monolayer, Int. J. Hydrogen Energy. 45 (2020) 18657–18665.

[48] M. Demirtas, M.J. Varjovi, M.M. Çiçek, E. Durgun, Tuning structural and electronic properties of two-dimensional aluminum monochalcogenides: Prediction of Janus Al 2 X X′(X/X′: O, S, Se, Te) monolayers, Phys. Rev. Mater. 4 (2020) 114003.

Reference

[49] B. Babariya, D. Raval, S.K. Gupta, P.N. Gajjar, Modulation of band gap and optical response of layered MoX2 (X = S, Se, Te) for electronic and optoelectronic applications, Mater. Today Commun. 28 (2021) 102614. https://doi.org/10.1016/j.mtcomm.2021.102614.

[50] A. Bafekry, S. Karbasizadeh, C. Stampfl, M. Faraji, D.M. Hoat, I.A. Sarsari, S.A.H. Feghhi, M. Ghergherehchi, Two-dimensional Janus semiconductor BiTeCl and BiTeBr monolayers: a first-principles study on their tunable electronic properties via an electric field and mechanical strain, Phys. Chem. Chem. Phys. 23 (2021) 15216–15223. https://doi.org/10.1039/D1CP01368H.

[51] M. Le Bellac, A short introduction to quantum information and quantum computation, Cambridge University Press, 2006.

[52] T. Raj, R. Shankar, M. Suhaib, A review of some issues and identification of some barriers in the implementation of FMS, Int. J. Flex. Manuf. Syst. 19 (2007) 1–40.

[53] H.F. Hameka, Quantum mechanics: a conceptual approach, John Wiley & Sons, Ltd, UK, 2004.

[54] J.J. Sakurai, E.D. Commins, Modern quantum mechanics, revised edition, (1995).

[55] D.D. Fitts, Principles of quantum mechanics: as applied to chemistry and chemical physics, Cambridge University Press, USA, 1999.

[56] W. Demtröder, Molecular physics: theoretical principles and experimental methods, Wiley-VCH Verlag GmbH&Co, USA., 2007.

[57] P.A.M. Dirac, Quantum mechanics of many-electron systems, Proc. R. Soc. London. Ser. A, Contain. Pap. a Math. Phys. Character. 123 (1929) 714–733.

[58] C.J. Cramer, Essentials of computational chemistry: theories and models, John Wiley & Sons, Ltd, UK, 2013.

[59] M. Born, R. Oppenheimer, Zur quantentheorie der molekeln, Ann. Phys. 389 (1927) 457–484.

[60] E.R. Bittner, J.B. Maddox, I. Burghardt, Relaxation of quantum hydrodynamic modes, Int. J. Quantum Chem. 89 (2002) 313–321.

[61] J. Kaminský, F. Jensen, Force field modeling of amino acid conformational energies, J. Chem. Theory Comput. 3 (2007) 1774–1788.

[62] S.M. Valone, Quantal Density Functional Theory II. Approximation Methods and Applications, (2010).

[63] T. Straßner, H.-J. Quadbeck-Seeger, S. Becker, H.H. Girault, D. Wöhrle, C.M. Niemeyer, D.G. Blackmond, G. Kaupp, T. Ziegler, S. Brakmann, Navigation Bar, Angew. Chem. 113 (2001) 4637–4639.

[64] D.W. Rogers, Computational Chemistry using the PC, John Wiley & Sons, Ltd, UK, 2003.

[65] M.E. Beck, M. Schindler, Quantitative structure–activity relations

based on quantum theory and wavelet transformations, Chem. Phys. 356 (2009) 121–130.

[66] R.M. Dreizler, E.K.U. Gross, Density functional theory: an approach to the quantum many-body problem, Springer Science & Business Media, 2012.

[67] G.G. Hall, The molecular orbital theory of chemical valency VIII. A method of calculating ionization potentials, Proc. R. Soc. London. Ser. A. Math. Phys. Sci. 205 (1951) 541–552.

[68] J. Hutter, Lecture notes in Computational Chemistry: Electronic Structure Theory, (2005).

[69] R.O. Jones, Introduction to density functional theory and exchange-correlation energy functionals, Comput. Nanosci. Do It Yours. 31 (2006) 45–70.

[70] W.J. Hehre, A guide to molecular mechanics and quantum chemical calculations, Wavefunction Irvine, CA, 2003.

[71] H. Dorsett, A. White, Overview of molecular modelling and ab initio molecular orbital methods suitable for use with energetic materials, Defense Science and Technology Organization Salisbury, Australia, 2000.

[72] P. Hohenberg, W. Kohn, Density functional theory (DFT), Phys. Rev. 136 (1964) B864.

[73] F. Jensen, Introduction to computational chemistry, John Wiley & Sons, Ltd, UK, Department of Chemistry, University of Southern Denmark, Odense, Denmark, 2017. https://doi.org/10.1360/zd-2013-43-6-1064.

[74] M.D. Weir, J.L. Moreau, E.D. Levine, H.E. Strassler, L.C. Chow, H.H.K. Xu, Nanocomposite containing CaF 2 nanoparticles: Thermal cycling, wear and long-term water-aging, Dent. Mater. 28 (2013) 642–652. https://doi.org/10.1016/j.dental.2012.02.007.

[75] K. Kim, K.D. Jordan, Comparison of density functional and MP2 calculations on the water monomer and dimer, J. Phys. Chem. 98 (1994) 10089–10094.

[76] V.E. Henrich, P.A. Cox, The surface science of metal oxides, Cambridge university press, 1996.

[77] C.E. Wagner, Exchange energy and potential using the Laplacian of the density, (2012).

[78] J.P. Perdew, K. Burke, M. Ernzerhof, Generalized Gradient Approximation Made Simple, Phys. Rev. Lett. 77 (1996) 3865–3868. https://doi.org/10.1103/PhysRevLett.77.3865.

[79] M. Sun, J.-P. Chou, J. Yu, W. Tang, Electronic properties of blue phosphorene/graphene and blue phosphorene/graphene-like gallium nitride heterostructures, Phys. Chem. Chem. Phys. (2017). https://doi.org/10.1039/C7CP01852E.

Reference

[80] J. Clark Stewart, D. Segall Matthew, J. Pickard Chris, J. Hasnip Phil, I.J. Probert Matt, K. Refson, C. Payne Mike, First principles methods using CASTEP, Zeitschrift Für Krist. - Cryst. Mater. 220 (2005) 567–570. https://doi.org/10.1524/zkri.220.5.567.65075.

[81] M.M. Obeid, H.R. Jappor, S.J. Edrees, M.M. Shukur, R. Khenata, Y. Mogulkoc, The electronic, half-metallic, and magnetic properties of Ca1-xCrxS ternary alloys: Insights from the first-principle calculations, J. Mol. Graph. Model. 89 (2019) 22–32. https://doi.org/10.1016/J.JMGM.2019.02.004.

[82] S. Grimme, Semiempirical GGA-type density functional constructed with a long-range dispersion correction, J. Comput. Chem. 27 (2006) 1787–1799.

[83] Y.-L. Wang, Y. Tian, Z.-L. Lang, W. Guan, L.-K. Yan, A highly efficient Z-scheme B-doped g-C3N4/SnS2 photocatalyst for CO2 reduction reaction: a computational study, J. Mater. Chem. A. 6 (2018) 21056–21063. https://doi.org/10.1039/C8TA07352J.

[84] M. Mousavi, A. Habibi-Yangjeh, M. Abitorabi, Fabrication of novel magnetically separable nanocomposites using graphitic carbon nitride, silver phosphate and silver chloride and their applications in photocatalytic removal of different pollutants using visible-light irradiation, J. Colloid Interface Sci. 480 (2016) 218–231. https://doi.org/10.1016/j.jcis.2016.07.021.

[85] J. Wang, Z. Guan, J. Huang, Q. Li, J. Yang, Enhanced photocatalytic mechanism for the hybrid g-C3N4/MoS2 nanocomposite, J. Mater. Chem. A. 2 (2014) 7960–7966. https://doi.org/10.1039/C4TA00275J.

[86] L. Ju, J. Shang, X. Tang, L. Kou, Tunable Photocatalytic Water Splitting by the Ferroelectric Switch in a 2D AgBiP2Se6 Monolayer, J. Am. Chem. Soc. 142 (2020) 1492–1500. https://doi.org/10.1021/jacs.9b11614.

[87] Y. Wei, Y. Ma, W. Wei, M. Li, B. Huang, Y. Dai, Promising Photocatalysts for Water Splitting in BeN2 and MgN2 Monolayers, J. Phys. Chem. C. 122 (2018) 8102–8108. https://doi.org/10.1021/acs.jpcc.8b01081.

[88] S. Yao, X. Zhang, Z. Zhang, A. Chen, Z. Zhou, 2D Triphosphides: SbP3 and GaP3 monolayer as promising photocatalysts for water splitting, Int. J. Hydrogen Energy. 44 (2019) 5948–5954. https://doi.org/10.1016/j.ijhydene.2019.01.106.

[89] L. Ju, M. Bie, X. Tang, J. Shang, L. Kou, Janus WSSe Monolayer: An Excellent Photocatalyst for Overall Water Splitting, ACS Appl. Mater. Interfaces. 12 (2020) acsami.0c06149. https://doi.org/10.1021/acsami.0c06149.

[90] H.T.T. Nguyen, T. V. Vu, N.T.T. Binh, D.M. Hoat, N.V.N. Hieu, N.T.T. Anh, C. V. Nguyen, H. V. Phuc, H.R. Jappor, M.M. Obeid,

Reference

N.V.N. Hieu, Strain-tunable electronic and optical properties of monolayer GeSe: Promising for photocatalytic water splitting applications, Chem. Phys. 529 (2020) 110543. https://doi.org/10.1016/j.chemphys.2019.110543.

[91] X. Gao, Y. Shen, Y. Ma, S. Wu, Z. Zhou, A water splitting photocatalysis: Blue phosphorus/g-GeC van der Waals heterostructure, Appl. Phys. Lett. 114 (2019) 093902. https://doi.org/10.1063/1.5082883.

[92] Z. Zhang, Q. Qian, B. Li, K.J. Chen, Interface Engineering of Monolayer MoS2/GaN Hybrid Heterostructure: Modified Band Alignment for Photocatalytic Water Splitting Application by Nitridation Treatment, ACS Appl. Mater. Interfaces. 10 (2018) 17419–17426. https://doi.org/10.1021/acsami.8b01286.

[93] Y. He, M. Zhang, J. Shi, Y. Cen, M. Wu, Improvement of Visible-Light Photocatalytic Efficiency in a Novel InSe/Zr2CO2 Heterostructure for Overall Water Splitting, J. Phys. Chem. C. 123 (2019) 12781–12790. https://doi.org/10.1021/acs.jpcc.9b01175.

[94] M.M. Obeid, A. Bafekry, S. Ur Rehman, C. V. Nguyen, A type-II GaSe/HfS2 van der Waals heterostructure as promising photocatalyst with high carrier mobility, Appl. Surf. Sci. 534 (2020) 147607. https://doi.org/10.1016/j.apsusc.2020.147607.

[95] S.M. Song, J.K. Park, O.J. Sul, B.J. Cho, Determination of Work Function of Graphene under a Metal Electrode and Its Role in Contact Resistance, Nano Lett. 12 (2012) 3887–3892. https://doi.org/10.1021/nl300266p.

[96] K. Ren, M. Sun, Y. Luo, S. Wang, J. Yu, W. Tang, First-principle study of electronic and optical properties of two-dimensional materials-based heterostructures based on transition metal dichalcogenides and boron phosphide, Appl. Surf. Sci. 476 (2019) 70–75. https://doi.org/10.1016/j.apsusc.2019.01.005.

[97] M. Zhou, W. Duan, Y. Chen, A. Du, Single layer lead iodide: computational exploration of structural, electronic and optical properties, strain induced band modulation and the role of spin–orbital-coupling, Nanoscale. 7 (2015) 15168–15174. https://doi.org/10.1039/C5NR04431F.

[98] Q. Wei, X. Peng, Superior mechanical flexibility of phosphorene and few-layer black phosphorus, Appl. Phys. Lett. 104 (2014) 251915. https://doi.org/10.1063/1.4885215.

[99] L. Tao, L. Huang, Computational design of enhanced photocatalytic activity of two-dimensional cadmium iodide, RSC Adv. 7 (2017) 53653–53657. https://doi.org/10.1039/C7RA09687A.

[100] D.M. Hoat, T. V. Vu, M.M. Obeid, H.R. Jappor, Tuning the electronic structure of 2D materials by strain and external electric

Reference

field: Case of GeI2 monolayer, Chem. Phys. 527 (2019) 110499. https://doi.org/10.1016/j.chemphys.2019.110499.

الخلاصة

في هذه الدراسة، أُستعمل برنامج استوديو المواد لتصميم مواد ثنائية الأبعاد AlBrSe و AlBrS أحادية الطبقة ذات التركيب الشبيكي رباعي قائم لأول مرة. دُرس تأثير الانفعال ثنائي على الخصائص التركيبية والكهروضوئية والتحفيز الضوئي لطبقات AlBrSe وAlBrSe الأحادية بواسطة نظرية الكثافة الوظيفية (DFT) باستخدام تقريب التدرج العام (GGA) مع الوظائف الهجينة (PBE) Perdew-Burke-Ernzerhof و Heyd-Scuseria-Ernzerhof (HSE). أشار منحنى تشتت الفونون ومحاكاة الديناميكيا الجزيئية إلى أن الطبقات الأحادية AlBrSe و AlBrS مستقرة ميكانيكيًا وديناميكيًا حراريًا مع عدم وجود قيم سالبة في الترددات.

لقد وجد أن الطبقة الاحادية AlBrSe هي شبه موصل ذو فجوة طاقة غير مباشرة تبلغ 1.654/2.231 eV بينما الطبقة الاحادية AlBrS تمتلك فجوة طاقة مباشرة تبلغ 2.221 eV/ 3.039 باستعمال طرق PBE و HSE06 على التوالي. تحت تأثير الانفعال، تتراوح فجوات الطاقة للطبقة الاحادية AlBrS من 1.837 إلى 2.353 eV بينما تتراوح فجوات الطاقة لطبقة AlBrS من 2.933 إلى 3.034 eV. ايضا، يمكن تعديل الخصائص الإلكترونية لطبقة AlBrSe أحادية الطبقة بشكل كبير تحت هندسة الانفعال، مع حدوث تحول كبير من فجوة الطاقة غير المباشرة إلى المباشرة خلال انفعال الشد (4٪ و6٪)، من جهة اخر فإن فجوات الطاقة المباشرة لطبقة AlBrS الأحادية تحافظ على موضعها عند النقطة Γ خلال الانفعال المطبق.

تقع القيمة القصوى لمعامل الامتصاص في المنطقة فوق البنفسجية للطبقتين الأحاديتين، بينما في المنطقة المرئية، يساوي معامل الامتصاص 6.13×10^{3} cm^{-1} عند طاقة 3.13 eV للطبقة الاحادية AlBrSe بينما يساوي $1.6\times10^{3}cm^{-1}$عند طاقة 3.15 eV للطبقة الأحادية AlBrS. كذلك تبلغ ذروة التوصيلية البصرية في الحالة الأصلية لـ AlBrSe حوالي $2.41 \times 10^{15}\ s^{-1}$عند طاقة 7.53 eV، بينما تساوي $3.65 \times 10^{-15}\ s^{-1}$ لـ AlBrS عند طاقة 7.83 eV.

تحت تأثير الإجهاد، يتصرف معامل الامتصاص والتوصيلية البصرية للطبقتين الأحاديتين بشكل مشابه: ينموان عند انفعال الكبس ويصلان إلى أعلى قيمه لهما عند 6-% ، وينخفضان عند انفعال الشد ويصلان إلى أدنى قيمه لهما عند 6٪. علاوة على ذلك، فإن استعمال الطبقات الأحادية AlBrSe وAlBrS في أنظمة الطاقة المبتكرة له مستقبل مشرق ومرشح واعد كمحفز ضوئي لتقسيم الماء.

جمهورية العراق
وزارة التعليم العالي والبحث العلـمي
جامعة بابل - كلية التربية للعلوم الصرفة
قســم الفـيزياء

تاثير الانفعال على الخصائص الإلكترونية والبصرية لطبقات (AlBrX) (X=S,Se) الأحادية

رسالة مقدمة
إلى مجلس كلية التربية للعلوم الصرفة في جامعة بابل وهي جزء من متطلبات
نيل درجة الماجستير في التربية / الفيزياء

من الطالب
سهاد طارق يوسف دهش
بكالـوريوس في الفيزياء
جامعة بغداد 2005 م

بإشراف كل من
أ.د. حمد رحمن جبر **أ. م. د. علي عبيس محسن**

1443 هـ **2022 م**